TIMCOAT: AN INTEGRATED FUEL PERFORMANCEMODEL FOR COATED PARTICLE FUEL

Jing Wang[a], Ronald G. Ballinger[a], Heather J. Maclean[a], Jane T. Diecker[a]
([a]Department of Nuclear Engineering, Massachusetts Institute of Technology, Cambridge MA 02139, USA)

ABSTRACT

An integrated fuel performance model for coated particle fuel has been developed to comprehensively study the behavior of TRISO coated fuel. Modeling of both pebble bed and prismatic configurations is possible. In the case of the pebble bed concept, refueling of pebbles is simulated to account for the non-uniform environment in the reactor core and history-dependent particle behavior. Monte Carlo sampling of particles is employed in fuel failure prediction to capture the statistical features of dimensions, material properties, and in the case of the pebble bed concept, the statistical nature of the refueling process. An advanced fuel failure model has been developed based on a probabilistic fracture mechanics approach. The mechanical analysis includes effects of anisotropic irradiation-induced dimensional changes and isotropic irradiation-induced creep, and fluence dependent Poisson's ratio in irradiation creep. The stress analysis is benchmarked against the calculations on Japanese High Temperature Test Reactor (HTTR) first-loading fuel and finite element result on one case performed by Idaho National Engineering and Environmental Laboratory (INEEL). The failure model predictions are compared with NPR1, NPR2, and NPR1A capsule irradiation data. The model results compare very favorably with PIE results both in terms of failure probability, number of failed particles and Kr^{85m} R/B evolution during irradiation.

1.0 INTRODUCTION

With the realization that nuclear power must play an important role in the future US and world energy mix, there has been a renewed interest in High Temperature Gas Reactors (HTGR) as potential sources for future energy needs. This interest is based the potential for a high degree of passive/inherent safety, achieved by the ability of the fuel system to quantitatively retain radiologically important fission products even at elevated temperatures and the promise of increased thermal efficiency over current Light Water Reactor (LWR) designs. Among HTGRs, the Modular Pebble-Bed Reactor (MPBR) and the Modular Helium Reactor (MHR) have received increased interest. Both designs make use of a coated particle fuel system which departs significantly from the pellet-in-fuel rod designs of other reactor types. The MPBR design uses coated fuel particles that are approximately 900 μm in diameter embedded in spherical graphite fuel "pebbles". An individual pebble contains roughly 15,000 coated particles within a graphite matrix in a spherical ball of 6 cm in diameter, which forms the fuel system. For a typical 120MWe reactor core design, there are approximately 360,000 pebbles. The pebbles, unlike the fuel rods in a conventional Light Water Reactor (LWR) which are stationary, move through the core on a continuous basis during operation. Partially burned and fresh fuel, when necessary, is added to the top of the core which has a geometry similar to that of a fluidized packed bed. Fuel pebbles then flow down through the core region. Upon exiting the core after a particular pass the pebbles are checked for accumulated burnup and integrity. Based on the results of this analysis a pebble is either removed from the stream and a new one added or it is recycled to the top (entrance) of the core for another cycle. Heat is transferred from the fuel to a gas, helium in most cases, flowing through the core. The MHR uses a more conventional stationary system in which the fuel particles are embedded in cylindrical fuel "compacts" which are then embedded in graphite fuel blocks. In addition to fuel, the fuel blocks also contain cooling passages and locations for absorber and control material. The MHR is refueled by periodic removal of depleted fuel blocks and the addition of

fresh fuel. Figures 1 and 2 show schematics of the fuel system for each type of reactor. Table 1 shows typical parameters for these two gas cooled reactor systems [1]. While the fuel particle design is identical in form for each of the two systems, the fuel system, moving pebbles vs. prismatic block, results in significant differences in fuel management and thus thermal history. In the pebble bed concept it is possible for a fresh pebble to be "inserted" into a location where the local fission power is also relatively high. This is the result of the random introduction, in terms of ultimate position in the core, of pebbles after a particular pass. As a result, the local peak to average power peaking factor in the fresh pebble can be relatively high compared to the prismatic design for the same nominal thermal conditions. Also, the fission power generated when a highly burned pebble is loaded in the vicinity of several fresh pebbles can "drive" more depleted fuel to higher temperatures than would otherwise be achieved based on its accumulated burnup. On the other hand, the fueling scheme in the stationary prismatic designs results in a steadily decreasing temperature with burnup during exposure due to both the fuel burnup and the fuel management scheme. Additionally, the more favorable heat transfer conditions in the pebble bed core, partially due to a lower power density, results in a peak temperature in the pebble bed design that is often several hundred degrees C lower than the peak temperature in a prismatic core.

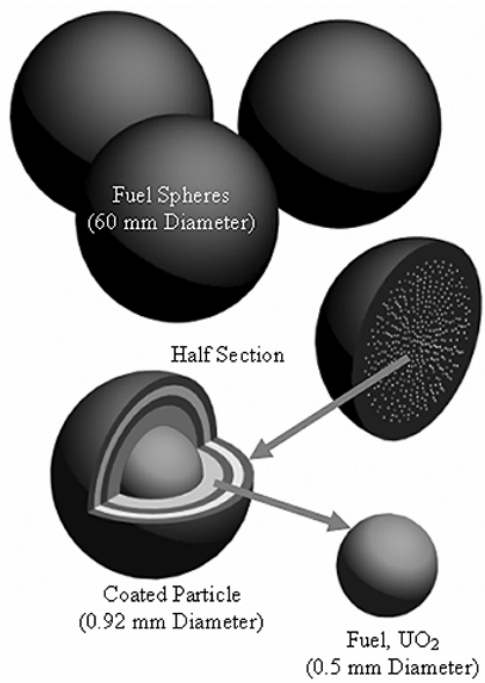

FIGURE 1. Schematic of the Pebble Bed fuel system. [PBMR Corp., with permission]

Figure 3 shows a schematic of a typical fuel particle. The fuel particles consist of a fuel kernel, typically UO_2, or UCO, surrounded by a series of graphite and ceramic layers [2]. The first coating is a low density, pyrolytic carbon (PyC) buffer layer. The purpose of the buffer layer is to absorb energy from fission product recoil and to provide void volume for accommodating gaseous fission products and other, chemically produced, gasses which may include CO or CO_2. The structural coatings following the buffer typically consist of a triple-layered composite material consisting of silicon carbide (SiC) sandwiched between dense PyC layers (called inner PyC (IPyC) and outer PyC (OPyC)). The resulting particles are termed TRISO fuel particles. In advanced fuel designs, the SiC layer has, in some cases, been replaced by ZrC. Figure 4 shows an actual TRISO particle [3]. In some cases there is a low-density PyC layer applied to the OPyC layer to protect the OPyC during fabrication of fuel compacts.

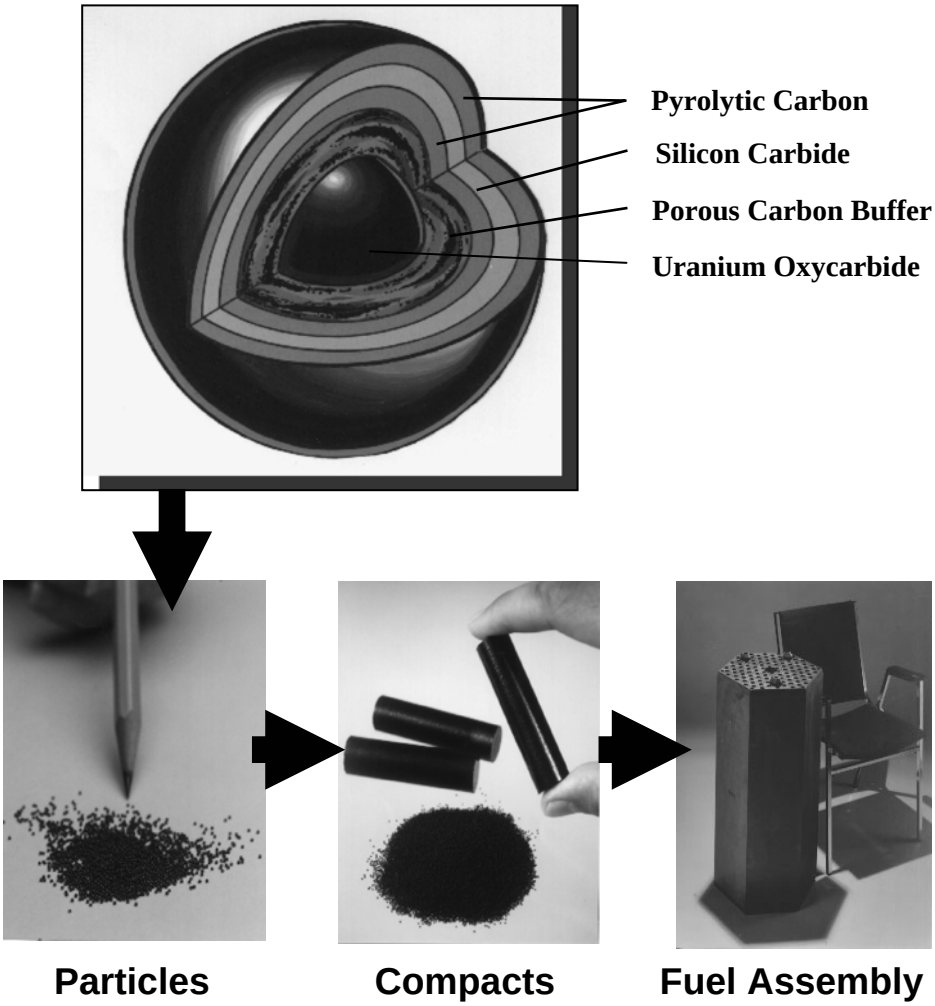

FIGURE 2. Schematic of the prismatic fuel system. [General Atomics Company, with permission]

The success of the gas cooled reactor concept relies heavily on the performance of the TRISO fuel particles. An argument has been made that due to the outstanding reliability of modern coated particle fuel, a containment as it is currently defined and required for LWR systems, may not be necessary [4]. The Fort St. Vrain reactor, a prismatic block design that was built and operated in the US during the 1970s and early 1980s, did not require a sealed containment but made use of a filtered, vented, confinement system. Beginning in the 1960s, the United States, Germany, France, and England developed gas cooled reactors for commercial and special material applications. The basic fuel concept evolved quickly to the current TRISO design and an extensive irradiation data base was developed. As part of this effort the performance of TRISO and other types of coated particle fuels has been extensively investigated and a number of models developed. Previously published fuel performance models have been largely developed in the US, the UK and Germany [5]. A detailed compilation of these models and other related topics has been published as an IAEA TECDOC [6]. These models included all aspects of particle fuel and gas reactor system performance. With respect to particle fuel performance specifically, many early models considered anisotropic irradiation-induced dimensional changes and isotropic irradiation-induced creep in inner and outer pyrocarbon layers, internal pressure buildup in the particle, and thermal expansion of structural layers. But as for failure, most of the previous models used a simple pressure vessel model and

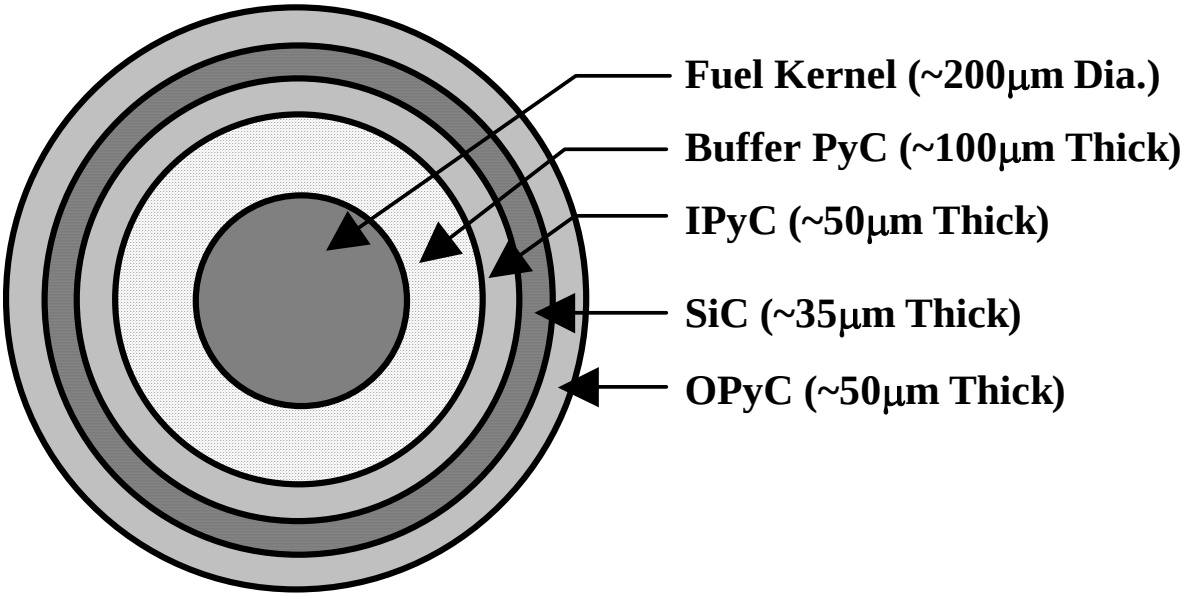

FIGURE 3. Coated particle fuel schematic.

Weibull statistics to account for layer strength distributions. The use of a pressure vessel failure model, in which failure occurs only when the fracture stress in a layer is exceeded, is a critical limitation even when a Weibull model for the fracture stress is used. Weibull statistics are often used to represent the effect of a distribution of internal flaws in a brittle material. To the extent that this represents the effect of internal flaws on the fracture behavior of pyrolytic carbon and SiC, use of a Weibull model is appropriate. However, failure is still assumed to be driven by the circumferential tensile stress in the layer. It has been shown in various works and will be in this paper that the stress in the SiC layer is compressive at least for the early irradiation period, typically for a fast neutron fluence of less than 2.0×10^{25}n/m^2 (E > 0.18 MeV). Hence, a pure pressure vessel failure model will not work in this fluence regime. Yet, fuel particle failures have been observed in experiments at an early stage of irradiation. At very high burnup and fast neutron fluence when internal pressure buildup is significant and the radial irradiation-induced strain in pyrocarbon layers turns to be positive, as shown in Fig. 10, all coating layers could be in tension and the pressure vessel model may take effect. The failure process for TRISO fuel during early irradiation is believed, and the microstructural data seems to support this, to be driven by cracking of the inner and/or outer pyrocarbon layer followed by cracking of the SiC layer. In this case, it is likely that the introduction of a sharp crack at the interface between the pyrocarbon and SiC (or ZrC) will result in a local stress concentration factor which may result in a locally high tensile stress even when the net section circumferential stress in the layer may still be compressive. Miller et al., [7] performed a more rigorous stress analysis for TRISO fuel and their results are being used in a fuel performance model being developed at the Idaho National Engineering and Environmental Laboratory (INEEL) [8]. The INEEL researchers also took a significant step in fuel failure modeling using finite the element method to evaluate local tensile stress in the SiC layer induced by a crack in the inner pyrocarbon layer. They compared the tensile stresses with SiC strength to determine failure [2]. However, this approach did not consider whether the size of the tensile stress zone at the tip of the crack is large enough to span a sufficient number of SiC grains so that the crack would, or could, grow into the SiC layer. Furthermore, local stresses calculated by the finite element method are very sensitive to the mesh size and shape and the type of crack

tip elements used. In this paper, we introduce a fracture mechanics approach for this problem, which automatically considers the level and the zone size for local stresses at a crack tip. It should be noted that, while the model reported here deals only with mechanically induced cracking, cracking of the pyrocarbon layer can also allow access for aggressive fission products (Cs, Pd, etc.) to the SiC which may then result in a stress concentration factor that can add additional duty to the fuel.

Table 1. Typical Gas Cooled Reactor Core Parameters

Parameter	Pebble-Bed (THTR)	HTGR (Ft. St. Vrain)
Thermal Power (MW)	300	842
Coolant	Helium	Helium
Core Inlet Temperature (°C)	250	405
Core Exit Temperature (°C)	750	775
Core Height (m)	6*	4.75*
Core Diameter (m)	5.6	5.9*
Number of Fuel Elements	675,000**	1482***
Fuel ElementDiameter (equivalent) (mm)	60	355
Fuel Element Length (equivalent) (mm)	-	787
Maximum Fuel Temperature (°C)	1250	1260
Average Burnup (MWd/kg)	109	100

* Active core parameters
** Pebbles
*** Fuel Elements

In addition to the use of a pressure vessel failure model, most earlier models assumed a more or less constant temperature exposure. However, many phenomena including irradiation induced dimensional changes, creep, chemical/thermodynamic phenomena and diffusion dependent phenomena such as fission product migration and release will depend on the fuel particle temperature history. In a Pebble-bed reactor the modeling of these phenomena requires that the complex non-isothermal environment in the reactor core be simulated. In the model reported here, for the first time, we incorporate the various analyses in a realistic reactor-core environment.

Early fuel performance models have, in some cases, showed good agreement with high-quality German fuel irradiation data in which the failure rate was very low. However, irradiation tests on New Production Reactor (NPR) fuel conducted at Idaho National Engineering & Environmental Laboratory (INEEL) and the Oak Ridge National Laboratory in 1991 and 1992 revealed unexpectedly high fuel particle failure rates with fuel made in the US but which was nominally similar to German fuel [5]. The higher failure rates were not predicted by either the German or the US fuel performance models at the time. The experience demonstrated, at least in part, that coated particle fuel behavior was not sufficiently well understood and that the existing fuel performance models were not able to adequately capture some of the most relevant physical phenomena in the particles during irradiation. Based on this less than satisfactory performance, it is clear that an improved fuel performance model is needed which tries to better represent the physics of fuel performance and the realistic irradiation environment.

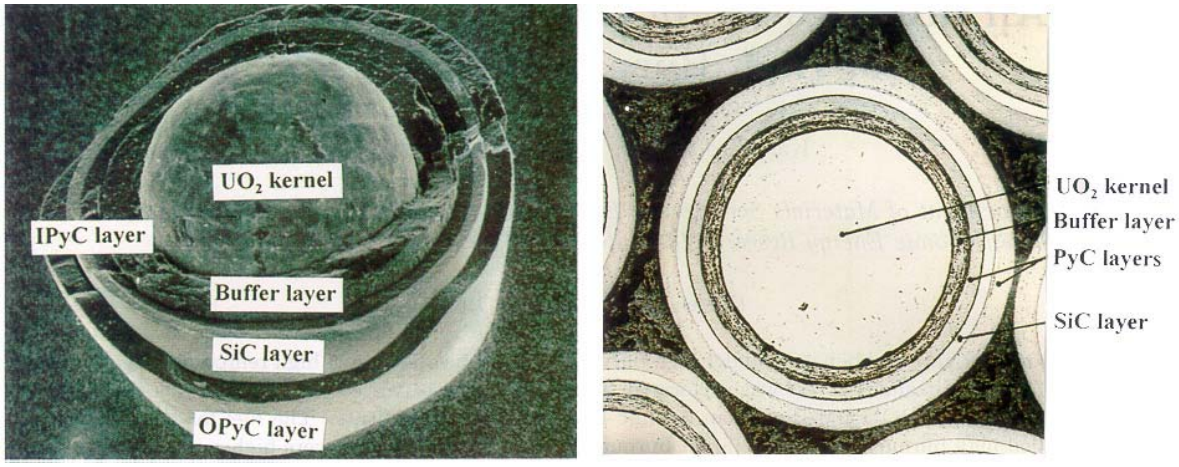

FIGURE 4. Coated particle fuel showing detailed features [3]

In this paper, we present a description of a new fuel performance model, TIMCOAT, developed at the Center for Advanced Nuclear Energy Systems (CANES) at MIT. While the ultimate model will treat all physical, chemical, irradiation and mechanical phenomena, the current version of the model focuses on the mechanical aspects of fuel performance and the mechanical failure of the barrier layers in the fuel particle. It will be shown that the dominant source of the stresses that produces failure of the barrier layers in the fuel particle are derived from the irradiation-induced shrinkage of the pyrocarbon layers. Fission gas induced pressure stresses and chemical interaction effects are minor contributors to the failure process except for: (1) very high burnup, (2) very high temperature operation or (3) operation where fuel kernel migration occurs. Future versions of the model will include a better fission gas release model given detailed treatment of fuel chemistry, and fission product attack of the SiC layer. For the model reported on in this paper the chemical description of the fuel environment is modeled in a simplified way and then only to derive the pressure from fission gas. A unique feature of the TIMCOAT model is the ability to model the Pebble-bed reactor refueling scheme as well as an ability to treat power histories for prismatic cores. Unlike prismatic core designs that were operated in the US and are now being operated in Japan, which use a fixed fuel system, the Pebble-bed reactor uses a multi-pass system, as has been discussed above, in which fuel is cycled through the bed several times prior to ultimate discharge. Fuel pebbles are extracted from the bottom of the core and then returned to the top of the bed. However, the location of the fuel pebble within a single pass is determined in a random manner based on the location of initial entry into the top of the bed. Thus, the modeling of the pebble-bed system requires that power histories for individual particles (associated with a particular pebble) be followed through these cycles. In the TIMCOAT model the refueling scheme is treated to simulate the real environment in the reactor core. To our knowledge this has not been considered in previously published models. The new model contains a detailed thermal analysis and incorporates fission gas production, swelling, and release models from the literature. However, with respect to the mechanical analysis of the pyrocarbon and ceramic layers, the new model contains an advanced mechanical model that extends the stress analysis by Miller et al. [7] to include a irradiation dependent Poisson's ratio in irradiation creep. Additionally, the modeling of fuel failure uses a different approach than those of previous models and is based on probabilistic fracture mechanics, in addition to the conventional Weibull strength model. The model can be used in the "single" power history mode or in the probabilistic mode in which fuel properties are sampled in a Monte Carlo simulation of the fuel irradiation process to predict the failure probability of fuel particles. As the main application to the fuel performance model in this paper we first "benchmark" our model against a finite

element calculation from INEEL and a model for High Temperature Test Reactor (HTTR) first-loaded fuel. We then compare the predictions of New Production Reactor (NPR) fuel performance with its irradiation data.. In the Results and Discussion section, the limitations of the current model and future enhancements are discussed.

2.0 DESCRIPTION OF THE TIMCOAT MODEL

The overall schematic and flow of the model is shown in Figure 5. Input power and neutron flux distributions are obtained from external sources. In the case of the pebble bed system, the power and neutron fluxes are obtained from the pebble bed VSOP code [9]. The details of this interface will be described below. Depending on the mode that is being run, either one or two Monte Carlo loops are employed. In cases where prismatic fuel is being evaluated, the outer Monte Carlo loop is employed to deal with the statistical nature of the fuel particle system. Fuel particle dimensions, and physical properties, where necessary, are input as statistical distributions. For a given individual input data set, the temperature distribution is then calculated and the fuel mechanically expanded to the operating temperature. Fission product and other fluence dependent parameters are then calculated for the time step. Fission gas release, pyrocarbon dimensional change and creep, temperature profile in the fuel particle and chemistry calculations are then combined with the mechanical analysis to obtain the mechanical and chemical state of the fuel particle. The output is then used by the failure model to determine fuel mechanical integrity which may include cracking of one or more of the barrier layers. If failure is detected the run is terminated in the single run mode. For the single run mode, if failure is not detected, the system recycles for the next time step until the end of life is achieved. For Monte Carlo simulations, the data for this particle is recorded, either after failure has occurred or after the end of life burnup is achieved and the system returns for another data set from the input distributions. For prismatic fuel analysis the number of trials depends on the anticipated failure probability for the fuel. As an example, if the anticipated failure probability is one particle in 10^5 then the minimum number of trials would be the order of 1-2 x 10^6. For a failure probability of one in 10^6 the number of trials must exceed 10^7 and probably 10^8. In the case of the pebble bed fuel system there is an additional Monte Carlo loop which samples the distribution of power histories associated with a random insertion of a partially burned pebble back into the core after each cycle. In the following sections a description of the individual models is provided.

2.1 THERMAL MODEL

The thermal calculation, while identical for each fuel system type once the particle surface temperature has been determined, is very different from the free stream gas temperature through either the prismatic block to a compact or to the pebble and individual particle. In the current version of the model it is assumed that in the case of a prismatic fuel system the temperature and power distributions are input to the model. For the pebble bed fuel system the power and flux distributions are obtained from VSOP for each individual fuel particle for each pass through the core. The temperature of the fuel particle is then calculated for each position as the fuel passes through the core. In this discussion we will focus on the pebble bed thermal calculation.

In the thermal model the pebble bed fuel particle temperature distribution is calculated for any position within the core. Since the fuel pebbles, in which the particles reside, travel through the core, the particle temperature distribution will be a function of time due to both its position during a particular pass through the core but also with time due to a particular path through the core for each pass. Since the path through the core is determined by the random introduction of the pebble at the top of the core, the actual temperature-time history of a particle cannot be known until the fuel is inserted at the top of the core. Figure 6 shows a schematic of the temperature profile calculation scheme. Given a known power distribution, both axially and radially, within the core, the helium mass flow rate, and the gas inlet temperature, the free stream gas temperature can be calculated as a function of position within the core.

Once the gas temperature is calculated the fuel pebble surface temperature can be calculated. After this, the temperature distribution within the pebble and within a specific fuel particle can be calculated.

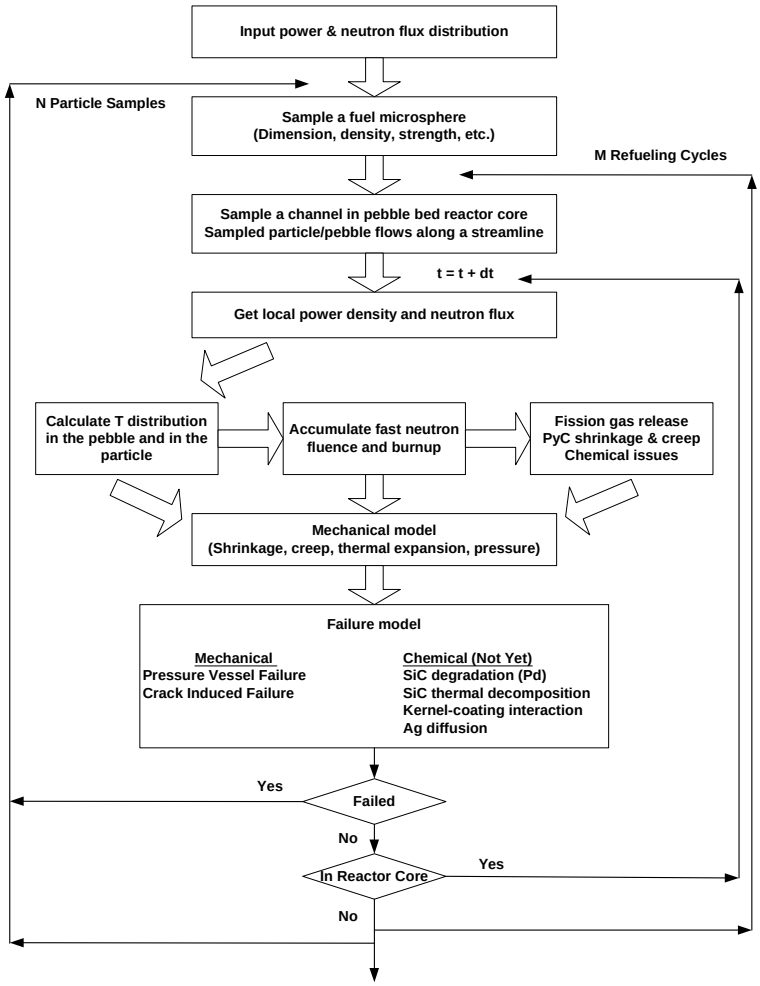

FIGURE 5. Schematic and flow diagram for MIT model.

2.1.1 GAS TEMPERATURE DISTRIBUTION AND PEBBLE SURFACE TEMPERATURE

The gas temperature at any location in the core is calculated knowing the gas inlet temperature and average volumetric heat generation rate as follows:

$$T_{He,bulk}(z) = T_{in} + \frac{q(z)}{\dot{m}\, c_{pHe}} \tag{1}$$

where T_{in} is the gas inlet temperature in °C, q(z) is the total heat added to the system to a height z per second, which can be calculated knowing the power distribution (volumetric heat generation rate), $\dot{m}$ is the helium mass flow rate (kg/s), and c_{pHe} is the helium specific heat (J/kg-°C). The local heat transfer coefficient h_{He} is calculated using the Achenbach correlation for the Nusselt number, Nu, as suggested by Dobranich [10] as follows:

$$Nu = \Pr^{1/3}\left[\left(1.18\,\mathrm{Re}^{0.58}\right)^4 + \left(0.23\,\mathrm{Re}^{0.75}\right)^4\right]^{0.25} = \frac{h_{He} d_p}{k_{He}} \tag{2}$$

where

$$\Pr_{He} = \frac{\mu_{He} c_{pHe}}{k_{He}},\ \mathrm{Re}_{He} = \frac{\rho_{He} V_{He} d_p}{\mu_{He}}, V_{He} = \frac{\dot{m}_{He}}{\rho_{He}\varepsilon_v A_c} \tag{3,4,5}$$

$$A_c = \frac{\left(n_{pebble} v_{pebble}\right) h_{core}}{1-\varepsilon_v} \tag{6}$$

n_{pebble} is the number of pebbles in the core,
v_{pebble} is the volume of a pebble (m^3),
h_{core} is the height of the core (pebble bed height in m),
ε_v is the core void fraction,
A_c is the core cross sectional area (m^2),
$\dot{m}$ is the helium mass flow rate (kg/s),
ρ_{He} is the helium density (kg/m^3),
V_{He} is the helium characteristic velocity (m/s),
d_p is the effective pebble diameter calculated by $d_p = 6\frac{v_{pebble}}{a_{pebble}}$ (m),
a_{pebble} is the surface area of a pebble (m^2),
μ_{He} is the viscosity of the helium (kg/m-s),
c_p is the specific heat of the helium (J/kg-°C),
k_{He} is the conductivity of the helium (W/m-°C),
$\Pr_{He}$ and Re_{He} are the Prandtl and Reynolds numbers for helium respectively.

The pebble surface temperature at any position in the core can then be calculated as follows:

$$T_{pbs} = \frac{q'''_{peb}}{3}\frac{r_{fz}^3}{r_{ps}^2}\frac{1}{h_{He}} + T_{He,bulk}(z) \tag{7}$$

where:
q'''_{peb} is the volumetric heat generation rate in a particular pebble (w/m^3)
r_{fz} is the fueled region radius in the pebble (m). (pebbles often have a fuel free region near the surface).
r_{ps} is the radius of the pebble (m).

2.1.2 PEBBLE AND FUEL PARTICLE TEMPERATURE DISTRIBUTION

A typical fuel pebble consists of a fueled region surrounded by a thin unfueled region at the surface. The fueled region consists of a graphite matrix surrounding several tens of thousands of fuel particles. A good approximation of the general temperature distribution in the pebble can be obtained by using volume averaged properties. The temperature at any location in the pebble can then be used to estimate the surface temperature of a particular fuel particle from which the temperature distribution within a particle can be calculated. The temperature at any position in the fuel pebble can be calculated by the following relationship:

$$T_{peb}(r) = T_{pbs} + \frac{q'''_{peb} r_{fz}^3}{3}\left[\frac{1}{k_{nfz}}\left(\frac{1}{r_{fz}} - \frac{1}{r_{ps}}\right) + \frac{1}{2k_{fz}}\left(\frac{1}{r_{fz}} - \frac{r^2}{r_{fz}^3}\right)\right] \tag{8}$$

for $0 \le r \le r_{fz}$

$$T_{peb}(r) = T_{pbs} + \frac{q'''_{peb} r_{fz}^3}{3}\left[\frac{1}{k_{nfz}}\left(\frac{1}{r} - \frac{1}{r_{ps}}\right)\right] \tag{9}$$

for $r_{fz} \le r \le r_{ps}$

where:
T_{pbs} is the pebble surface temperature (°C)
r_{fz} is the radius of the fueled region of the pebble (m)
r_{ps} is the pebble radius (m)
k_{nfz} is the volume average conductivity of the non-fueled region of the pebble (W/m-°C)
k_{fz} is the volume average conductivity of the fueled region of the pebble (W/m-°C).

The volume averaged conductivity of the fueled region of the pebble is calculated as follows:

$$k_{fz} = \frac{1}{V_{fz}}\left(V_f k_f + V_b k_b + V_g k_g + V_I k_I + V_S k_S + V_O k_O + V_{fzm} k_{fzm}\right) \tag{10}$$

where:

V_f, V_b, V_g, V_I, V_S, V_O, and V_{fzm} are the volumes of the fuel, buffer, any gas gap that may form in the fuel particles during irradiation, IPyC, SiC (or ZrC), OPyC and graphite within the fuel zone of the pebble respectively. Additionally, k_f, k_b, k_g, k_I, k_S, k_O, and k_{fzm} are the corresponding conductivities which will be a function of temperature, burnup in the case of the fuel and any gas gap that develops as the buffer shrinks during exposure, and fluence. k_{nfz} is the volume averaged conductivity of the non-fueled outer graphite layer.

Within an individual fuel particle the temperatures within individual particle layers can be determined knowing the particle surface temperature (from the pebble temperature at the location of the particle within the pebble), the volumetric heat generation rate in the particle and boundary conditions, listed in Table 2. We assume that the temperature is symmetric about the particle center which is a simplification since, in fact, there will be a gradient due to the temperature distribution in a pebble and, indeed, this temperature distribution will also not be symmetric. However, the effect of this assumption will be minor since the actual temperature drop within pebbles will be on the order of 50°C from center to pebble surface. From a chemistry point of view it is not the temperature gradient within a pebble that is important, but the temperature gradient within an individual particle. Solution of the heat conduction problem yields the following relationships for the temperature distribution:

$$T(r) = \frac{q'''_f r_f^3}{3}\left[\frac{1}{k_O}\left(\frac{1}{r_S} - \frac{1}{r_O}\right) + \frac{1}{k_S}\left(\frac{1}{r_I} - \frac{1}{r_S}\right) + \frac{1}{k_I}\left(\frac{1}{r_g} - \frac{1}{r_I}\right) + \frac{1}{k_g}\left(\frac{1}{r_b} - \frac{1}{r_g}\right) + \frac{1}{k_b}\left(\frac{1}{r_f} - \frac{1}{r_b}\right) + \frac{1}{2k_f}\left(\frac{1}{r_f} - \frac{r^2}{r_f^3}\right)\right] + T_{pars} \tag{11}$$

for $0 \le r \le r_f$

$$T(r) = \frac{q'''_f r_f^3}{3}\left[\frac{1}{k_O}\left(\frac{1}{r_S} - \frac{1}{r_O}\right) + \frac{1}{k_S}\left(\frac{1}{r_I} - \frac{1}{r_S}\right) + \frac{1}{k_I}\left(\frac{1}{r_g} - \frac{1}{r_I}\right) + \frac{1}{k_g}\left(\frac{1}{r_b} - \frac{1}{r_g}\right) + \frac{1}{k_b}\left(\frac{1}{r} - \frac{1}{r_b}\right)\right] + T_{pars} \tag{12}$$

for $r_f \le r \le r_b$

$$T_{par}(r) = \frac{q_f''' r_f^3}{3}\left[\frac{1}{k_O}\left(\frac{1}{r_S}-\frac{1}{r_O}\right)+\frac{1}{k_S}\left(\frac{1}{r_I}-\frac{1}{r_S}\right)+\frac{1}{k_I}\left(\frac{1}{r_g}-\frac{1}{r_I}\right)+\frac{1}{k_g}\left(\frac{1}{r}-\frac{1}{r_g}\right)\right]+T_{pars} \tag{13}$$

for $r_b \le r \le r_g$

$$T_{par}(r) = \frac{q_f''' r_f^3}{3}\left[\frac{1}{k_O}\left(\frac{1}{r_S}-\frac{1}{r_O}\right)+\frac{1}{k_S}\left(\frac{1}{r_I}-\frac{1}{r_S}\right)+\frac{1}{k_I}\left(\frac{1}{r}-\frac{1}{r_I}\right)\right]+T_{pars} \tag{14}$$

for $r_g \le r \le r_I$

$$T_{par}(r) = \frac{q_f''' r_f^3}{3}\left[\frac{1}{k_O}\left(\frac{1}{r_S}-\frac{1}{r_O}\right)+\frac{1}{k_S}\left(\frac{1}{r}-\frac{1}{r_S}\right)\right]+T_{pars} \tag{15}$$

for $r_I \le r \le r_S$

$$T_{par}(r) = \frac{q_f''' r_f^3}{3}\left[\frac{1}{k_O}\left(\frac{1}{r}-\frac{1}{r_O}\right)\right]+T_{pars} \tag{16}$$

for $r_S \le r \le r_O$

where

T_{pars} is the particle surface temperature at the location within the pebble where the particle resides, q_f''' is the volumetric heat generation rate in the particle and dimensions are defined in Figure 7. Also shown in Figure 7 are typical temperature distributions within both a pebble and an individual particle located at the center of the pebble.

Figure 8 shows plots of the thermal conductivities used in the model as a function of temperature. The conductivity for UO_2, layer and buffer pyrocarbon, SiC, matrix graphite, and helium are from El-Wakil [11], Dobranich [10], Price [12], Kania and Nickel [13], and Mills [14], respectively.

Table 2. Particle Thermal Boundary Conditions

Position	**Heat Flux**	**Temperature**
$r = 0$	$dq_f/dr = 0$	
$r = r_f$	$q_f(r_f) = q_b(r_f)$	$T_f(r_f) = T_b(r_f)$
$r = r_b$	$q_b(r_b) = q_i(r_b)$	$T_b(r_b) = T_i(r_b)$
$r = r_i$	$q_i(r_i) = q_s(r_i)$	$T_i(r_i) = T_s(r_i)$
$r = r_s$	$q_s(r_s) = q_o(r_s)$	$T_s(r_s) = T_o(r_s)$
$r = r_o$		$T_o(r_o) = T_{pars}$

2.2 FISSION GAS RELEASE

The fission gas release model is based on a model developed at the University of Tennessee (UT) and the Institute for Safety Research and Reactor Technology at the Research Center in Germany (KFA) [15]. The release of long-lived fission gases from the kernel is described by diffusion driven transport from a sphere, written mathematically as

$$\frac{\partial C}{\partial t} = \frac{D}{r^2}\left[\frac{\partial}{\partial r}\left(r^2 \frac{\partial C}{\partial r}\right)\right] + S\,, \tag{17}$$

where:

C is the fission product concentration (atoms.m^{-3}),
D is the diffusion coefficient (m^2/s),
S is the uniform source of fission product (atoms.m^{-3}·s^{-1}).

The analytical solution of Equation (17) is obtained given proper initial and boundary conditions. As shown in Figure 3, fission gases are generated from the fuel kernel and partially released into the buffer layer. If initially there is no fission gas in the kernel and buffer layer, and the generation of fission products is homogeneous in the kernel, then the fractional gaseous release is given in Eqn (18) [16]. If the fuel is irradiated for a time t_i (s) at temperature T_i (K) and after irradiation is heated for time t_a (s) at temperature T_a (K), the fractional release F_d during irradiation is calculated by Eqn 19,which yields the overall release of fission gases less the release during annealing.

$$f(\tau) = 1.0 - \frac{6}{\tau}\sum_{n=1}^{\infty}\frac{\left[1-\exp\left(-n^2\pi^2\tau\right)\right]}{n^4\pi^4}\,, \tag{18}$$

$$F_d = \frac{(\tau_i+\tau_a)\,f(\tau_i+\tau_a) - \tau_a f(\tau_a)}{\tau_i}\,, \tag{19}$$

and

$$\tau_i = DS(T_i)\,t_i\,, \tag{20}$$

$$\tau_a = DS(T_a)\,t_a\,, \tag{21}$$

where DS is the reduced diffusion coefficient (s^{-1}) of the fission gases in the particle kernel given by $DS = D_{eff} / r^2$ with D_{eff} which is the effective diffusion coefficient and r being the kernel radius. For UO_2 kernels, DS is given by [15]

$$DS = \exp(-5.29 - 18690/T)\,. \tag{22}$$

If there is no annealing involved, it can be seen from Eqn 19 that F_d is simply $f(\tau_i)$.

In addition to fission gases, oxygen atoms are also released as a result of fission in UO_2 kernels. The number of oxygen atoms released per fission (OPF) is calculated based on empirical relationships derived from mass-spectrometric measurements of CO in irradiated UO_2 fuel particles [15]. During irradiation, the equation is

$$\log(OPF) = -10.08 - 8500/T_i + 2\log(t_i) \tag{23}$$

and during heating, it is

$$\log(OPF) = -10.08 - 8500/T_i + 2\log(t_i) - 4.04\left[(1000/T_a) - 1000/(T_i+75)\right]. \tag{24}$$

The internal gas pressure p (Pa) is determined by the ideal gas law in the following manner,

$$pV_f = \left[\left(F_d F_f + OPF\right)F_b\left(V_k/V_m\right)\right]RT\,, \tag{25}$$

where:

V_f is the void volume (m^3),
F_f is the gaseous fission product yield,
F_b is the heavy metal burnup (FIMA),

V_k is the kernel volume (m^3),
V_m is the molar volume of kernel (m^3/mol),
R is the ideal gas constant (8.31J/mol·K),
T is the temperature (°K).

Equations (18), (23) and (24) are only valid for isothermal conditions either during irradiation or during post irradiation heating tests. Therefore when running the model using power histories, the current version omits consideration of diffusion by assuming 100% gas release from kernels ($F_d = 1$). Diffusive release is only considered for isothermal irradiations. Future versions of the model will implement a more sophisticated fission gas release model that can be used with arbitrary temperature-time histories.

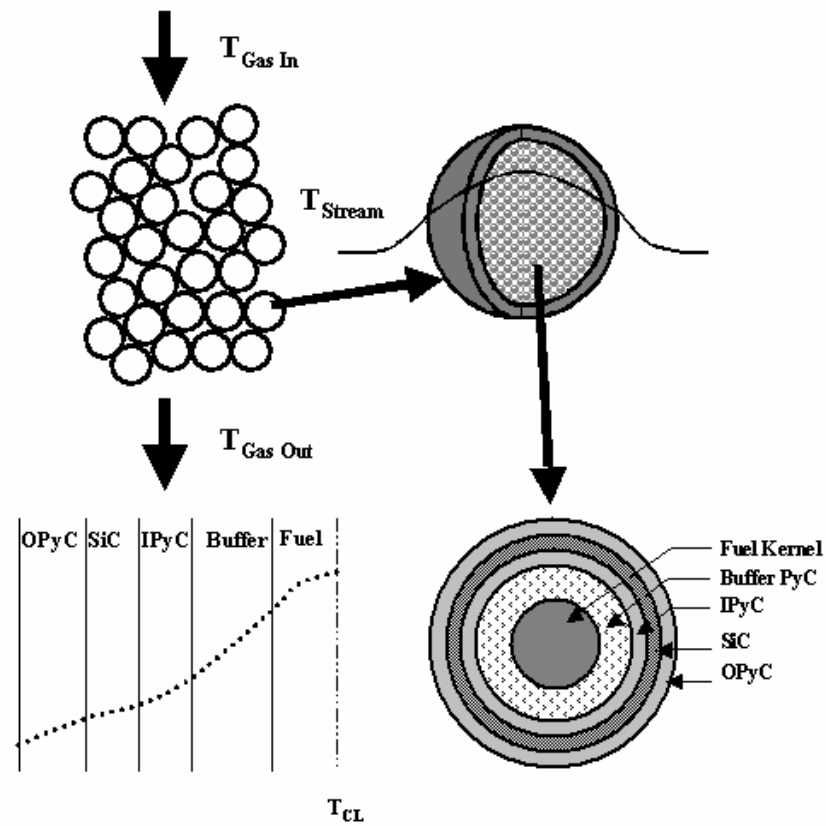

FIGURE 6. Schematic of the pebble thermal analysis flow path.

2.3 Mechanical Analysis

The mechanical analysis uses a viscoelastic model for the pyrolytic carbon layers and follows the technique described by Miller et al. [7] in analyzing stresses in TRISO coatings. In the TIMCOAT model we extend their solution by the allowance of a variable Poisson's ratio in irradiation creep. The stress-strain relations in the radial and tangential directions for the spherical geometry of the pyrolytic carbon layers (IPyC and OPyC) are:

$$\frac{\partial \varepsilon_r}{\partial t} = \frac{1}{E}\left(\frac{\partial \sigma_r}{\partial t} - 2\nu \frac{\partial \sigma_t}{\partial t}\right) + c\left(\sigma_r - 2\nu_c \sigma_t\right) + \dot{S}_r \tag{26}$$

$$\frac{\partial \varepsilon_t}{\partial t} = \frac{1}{E}\left[\left(1-\nu\right)\frac{\partial \sigma_t}{\partial t} - \nu\frac{\partial \sigma_r}{\partial t}\right] + c\left[\left(1-\nu_c\right)\sigma_t - \nu_c\sigma_r\right] + \dot{S}_t \tag{27}$$

where:
ε_r, ε_t are the strains in the radial or tangential directions,
σ_r, σ_t are the stresses in the radial or tangential directions (MPa),
c is the pyrocarbon creep coefficient (10^{-21}cm^2/Pa),
$\dot{S}_r$, $\dot{S}_t$ are the Irradiation dimensional change rate of PyC in the radial or tangential direction (10^{-21} cm^2),
ν_c is Poisson's ratio in irradiation creep,
E is the Young's modulus (MPa),
ν is Poisson's ratio.

Assuming perfect spherical shape for the layers, we can write the strain-displacement relations and equations of equilibrium as follows:

$$\varepsilon_r = \frac{\partial u}{\partial r}, \tag{28}$$

$$\varepsilon_t = \frac{u}{r}, \tag{29}$$

$$\frac{\partial \sigma_r}{\partial r} + \frac{2}{r}\left(\sigma_r - \sigma_t\right) = 0. \tag{30}$$

where:
u is the radial displacement (μm).

To solve equations (26) through (30), we use a series solution:

$$u\left(r,t\right) = \sum_{i=0}^{\infty} u_i(r)t^i, \tag{31}$$

$$\sigma_r\left(r,t\right) = \sum_{i=0}^{\infty} \sigma_{ri}(r)t^i, \tag{32}$$

$$\sigma_t\left(r,t\right) = \sum_{i=0}^{\infty} \sigma_{ti}(r)t^i, \tag{33}$$

$$\dot{S}_r\left(t\right) = \sum_{i=0}^{\infty} \dot{S}_{ri}\, t^i,\ \dot{S}_t\left(t\right) = \sum_{i=0}^{\infty} \dot{S}_{ti}\, t^i. \tag{34}$$

The final solution takes the form:

$$u_{i+1}(r) = A_{i+1}r + B_{i+1}r^{-2} + \frac{2(k-m)}{3} f_{i+1} r \ln r, (i \geq 0) \tag{35}$$

$$\sigma_{ri+1}(r) = \frac{A_{i+1}}{k-m} - \frac{2B_{i+1}}{l+m}r^{-3} + 2f_{i+1}\frac{\left[\left(l+m\right)\ln r + k\right]}{3\left(l+m\right)}$$
$$-\frac{c}{l+m}\frac{1}{(i+1)}\left\{\left[1+\frac{m(1-2\nu_c)}{k-m}\right]\sigma_{ri} + \left[\frac{l(1-2\nu_c)}{k-m} - 1\right]\sigma_{ti}\right\} - \frac{k\dot{S}_{ri} + h\dot{S}_{ti}}{(i+1)(kl-hm)}, (i \geq 0) \tag{36}$$

$$\sigma_{ti+1} - \sigma_{ri+1} = \frac{3B_{i+1}}{l+m}r^{-3} - \frac{2f_{i+1}(k-m)}{3(l+m)} + \frac{3c}{2(l+m)}\frac{1}{(i+1)}\left[\frac{2(1+\nu_c)}{3}\left(\sigma_{ri} - \sigma_{ti}\right)\right] + \frac{\dot{S}_{ri} - \dot{S}_{ti}}{(i+1)(l+m)}, (i \geq 0) \tag{37}$$

where:

A_i, B_i are coefficients to be solved for by applying boundary conditions,

$$l = \frac{1}{E},\ h = \frac{2\nu}{E},\ m = \frac{\nu}{E},\ k = \frac{1-\nu}{E},$$

$$f_{i+1} = -\frac{c}{2k}\frac{2(l\nu_c - m)}{k-m}\frac{g_i}{i+1} + \frac{\dot{S}_{ri} - \dot{S}_{ti}}{k(i+1)}, (i \geq 0) \tag{38}$$

$$g_{i+1} = f_{i+1} - \frac{c(1-2\nu_c)}{(i+1)(k-m)} g_i, (i \geq 0) \tag{39}$$

$$g_0 = 0.$$

The pyrocarbon creep coefficient, c (10^{-21} cm^2/MPa), is from [17] and is defined as:

$$c = \left[1 + (1.9 - \rho) \times 2.38\right] \times \left[2.193 \times 10^{-4} - 4.85 \times 10^{-7} T + 4.0147 \times 10^{-10} T^2\right] \tag{40}$$

where ρ is the density in gm/cm^3 and T is the temperature in °C.

The above provides for an explicit time-dependent solution to the problem, from which we can obtain stress profiles through the layers at any time. In this analysis, residual stresses are able to be accounted for by σ_{r0} and σ_{t0} (when i =0), and they affect higher order terms and, therefore, the entire stress history. The above solution technique allows the model to deal with any power history.

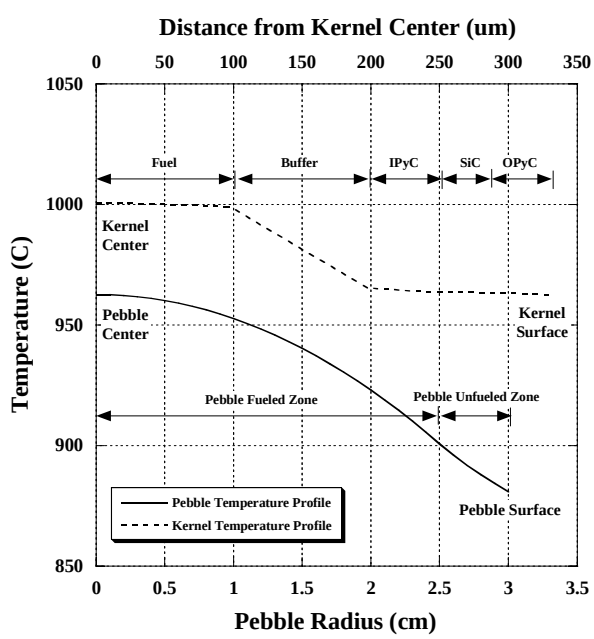

FIGURE 7. Fuel and pebble dimensions and temperature distributions.

The solution presented here uses the same visco-elastic model for pyrocarbon and equation solving technique as those by Miller, et al. [7], but since Poisson's ratio in irradiation creep ν_c is not assumed to be

0.5 in this case, the solutions in Eqns 35 through 39 take different forms. In fact, the solutions here collapse into the solutions given by Miller, et al., if ν_c is fixed at 0.5. The physical meaning of this special value is that pyrocarbon is treated as an incompressible medium when dealing with creep. It was shown in the work by Miller, et al. that their series solution could be cast into an exact closed form solution, which is faster than the series solution for performing calculations using the Monte Carlo method, but that is no longer achievable if ν_c is allowed to vary, primarily because of the presence of some ν_c dependent terms as shown in Eqns 36 through 39. It should be pointed out that the value of Poisson's ratio in creep will have a strong influence on the stress levels in the coating layers during exposure, as will be shown in the stress comparison section below. In the TIMCOAT model we have chosen to allow the creep Poisson's ratio to vary with fluence as suggested by Kaae [18]. Figure 9 shows the data from Reference [18].

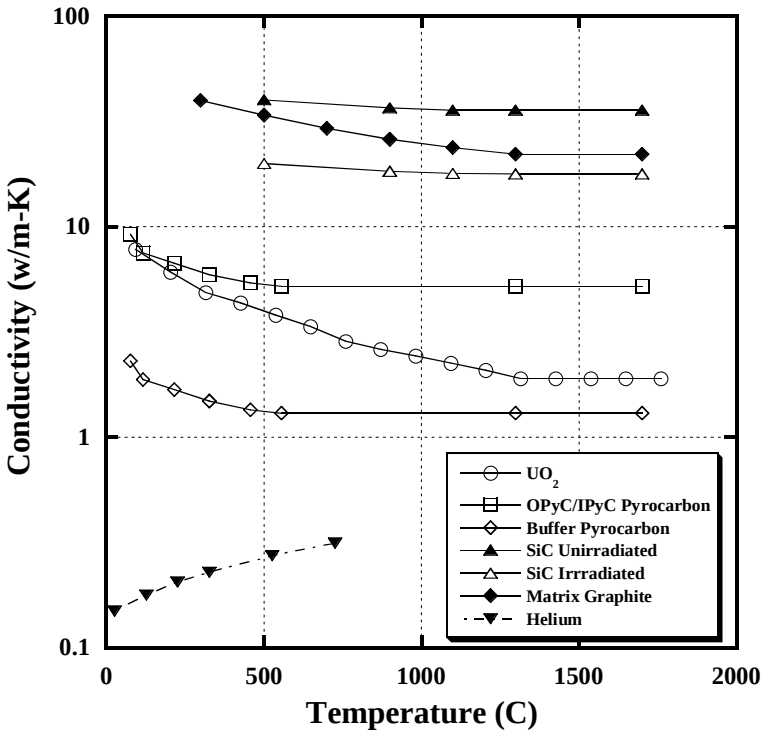

FIGURE 8. Conductivity data for thermal model [10-14].

2.4 PYROCARBON SWELLING

The key factor in the evolution of stresses in the layers is the behavior of the pyrocarbon during irradiation. The properties of chemical vapor deposited (CVD) pyrocarbon depend on several variables including the feed gas type, concentration, temperature and pressure during deposition which, in turn, determines the rate of deposition [19]. The extent of anisotropy in the pyrocarbon is represented by the Bacon Anisotropy Factor (BAF) which is a measure of the ratio of the fraction of graphite crystallites oriented parallel to those oriented perpendicular to the c-axis in the graphite unit cell. The irradiation behavior of the pyrocarbon will depend on the initial BAF number. More importantly, the BAF number

will change with irradiation exposure. Figure 10 shows the swelling behavior of pyrocarbon for initial BAF numbers of 1.036 and 1.063. A BAF value of 1.063 is considered fairly large for current fuel. A complete family of curves for a range of BAF numbers has been developed from data developed as part of the New Production Reactor program [20]. The difference between a BAF_0 of 1.036 and 1.063 amounts to a factor of two in swelling strain, a shift in the point of minimum tangential swelling strain to higher fluence for the lower BAF, and generally less "steep" behavior of the swelling strain rate as a function of fluence. This behavior will translate into lower pyrocarbon stresses at a given temperature and a shift to higher fluence of the point of maximum pyrocarbon stress during irradiation for the lower BAF_0. Since the particle average temperature will tend to decrease with burnup, this will then result in lower failure probabilities and an increase in the time to the point of maximum vulnerability of the fuel-the point of maximum tangential stress- to failure as well as a general decrease in vulnerability at the point of maximum stress.

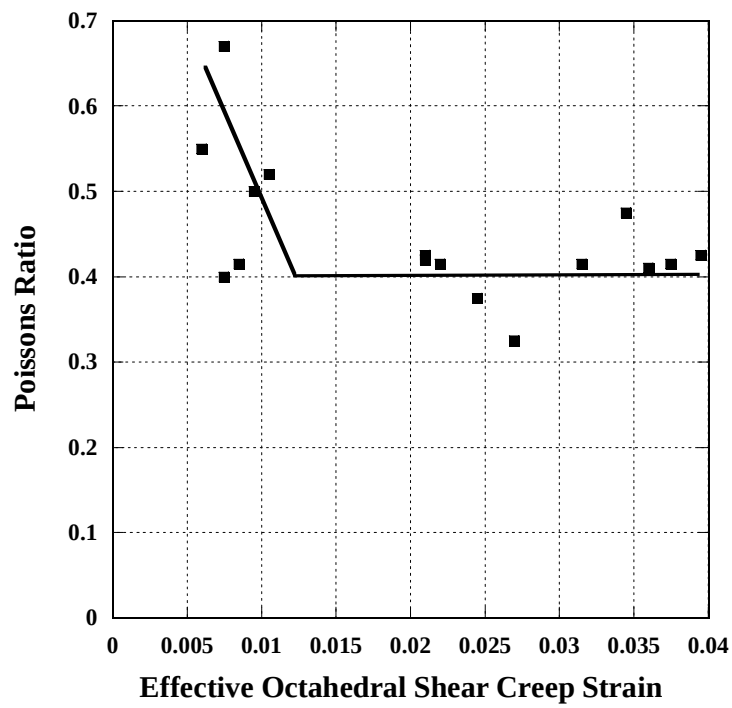

FIGURE 9. Creep Poisson's ratio for pyrocarbon [18].

2.5 FAILURE MODELS

The classical pressure vessel failure model, which is used by most of the previously published coated particle fuel performance models, is not adequate to characterize all of the potential mechanical fuel failure mechanisms in that it only considers uniform circumferential tension in an intact spherical fuel particle as the source of failure. If there is a crack or large defect in one of the layers, in particular the inner pyrocarbon layer, there is the possibility that an increased localized stress may be produced that will impact the fracture of the SiC layer. As we mentioned in the Introduction section, Miller et al. [2] took

into account the effect of IPyC shrinkage crack on overall particle failure by finite element stress calculation for the first time, but a fracture mechanics approach is more appropriate to treat such a failure mechanism. The application of fracture mechanics provides a means by which the effect of a localized stress can be accounted for. Specifically, the TIMCOAT model uses the stress intensity factor to characterize the local stresses caused by a crack in one (or both) of the PyC layers. A schematic of the cracking induced failure process is shown in Figure 11.

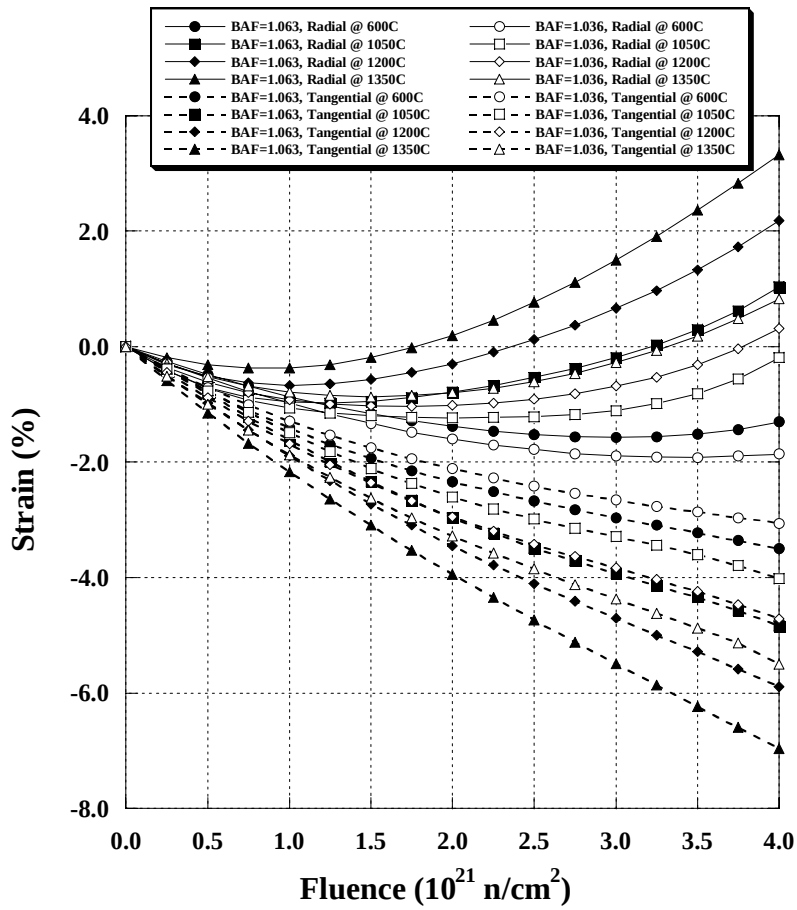

FIGURE 10. Typical swelling behavior for pyrocarbon as a function of fluence for initial BAF values of 1.036 and 1.063 [20].

During operation the source of stresses in the layers include: (1) differential thermal expansion of the individual layers, (2) internal gas pressure, (3) external system pressure, and (4) layer stresses that result from irradiation induced dimensional changes and creep of the PyC. For typical particle fuel fabrication processes the PyC layers (both inner and outer) undergo a net circumferential shrinkage during exposure. The result of this is that, for most fuel designs, the PyC layers are placed in net circumferential tension while the SiC (which does not change dimension appreciably during exposure) is placed in net circumferential compression. The effect of internal gas pressure is small compared to the shrinkage-induced stresses except for very high burnups when there will be significant fission gas release or if the particle dimensions are such that the ratio of layer diameter to thickness is very large. If the

circumferential tensile stress in the PyC layer exceeds its fracture strength a radial crack will develop. The through-IPyC-layer crack ("a" in Figure 11) will result in an increase in the local stress at the PyC/SiC interface and will produce a local crack tip stress intensity that is defined by the crack tip stress intensity factor, K. If the value of K exceeds the fracture toughness (K_{IC}) of the SiC layer then the layer will fail even when the far field stress in the SiC is compressive. Once the SiC layer is failed, we assume the remaining intact PyC layer, if there is one, will also be cracked. Hence this version of the failure model will give the same SiC layer failure probability as the overall particle failure probability. We term this model the "Crack Induced Failure Model (CIFM)". Since the fuel coating materials are brittle, the use of Linear Elastic Fracture Mechanics (LEFM) is valid to at least first order for this application. In the current version of the model the application of LEFM to the failure process is highly simplified and makes the following assumptions: (1) the crack tip stress intensity factor is calculated assuming that the layer properties (elastic modulus, etc.) are the same. That is, no account is taken for the composite nature of the geometry, (2) SiC layer failure is assumed to occur coincidently with the cracking of the PyC layer. No account is taken for the further evolution of local stresses due to continued PyC shrinkage after failure. The result of the first assumption is that the effect of the difference in elastic modulus between the SiC and pyrocarbon layers is not accounted for. The lower modulus of the pyrocarbon will be likely to result in a higher than actual prediction of the radial crack induced stress intensification. Additionally, since we are, in effect, treating the system as a continuum, the possibility of non-radial cracks developing is also not accounted for. The effect of the second assumption is to eliminate the possibility that pyrocarbon cracks that do not cause instantaneous failure of the SiC layer might result in future failure due to continued shrinkage-induced stress buildup. This may have a significant negative effect on the overall failure probability prediction. Future versions of the model will account for shape and multi-layer effects as well as further history effects. In this paper we simply seek to introduce the concepts and to demonstrate the value of this approach.

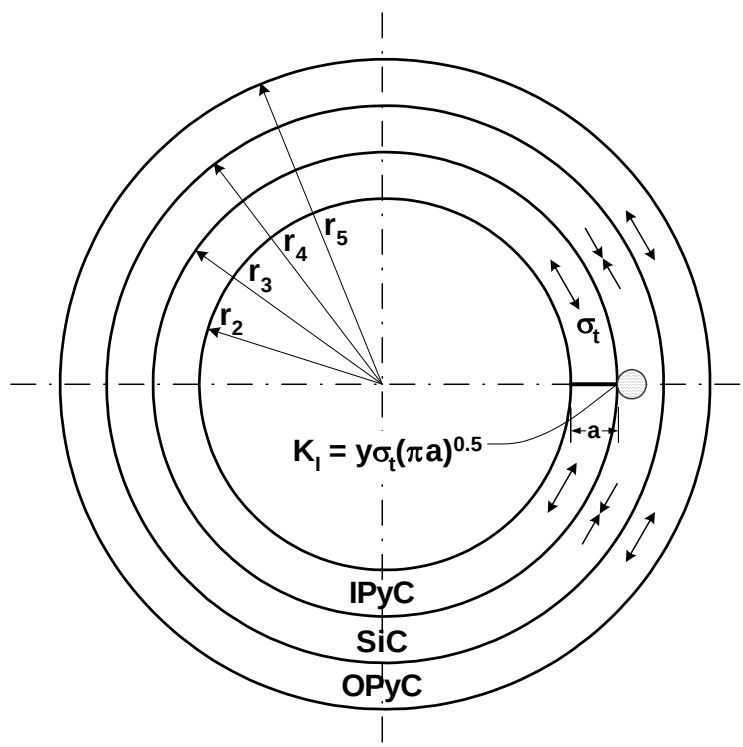

FIGURE 11. Schematic for fracture mechanics model of fuel failure.

2.6 PEBBLE-BED FUELING SCHEME

As discussed earlier, the pebble-bed reactor fueling scheme consists of a number of cycles, typically 10-15, where a particular pebble is fed to the top of the core in a random manner. Once the pebble is introduced it will follow a streamline that is defined, to first order, by the location of entry. The core shape can be approximated by a right circular cylinder with a cone-shaped exit region. Fuel pebbles flow through the system in much the same way that sand flows through an hourglass. When a pebble exits the core its burnup and failure status are checked. If the end of life burnup has not been reached and the pebble contains no failed fuel particles it is recycled to the top of the core where it is introduced once again. However, the ultimate streamline that the pebble follows during a particular pass through the core is independent of the streamline for previous and subsequent passes. Thus, the actual power history for a particular fuel particle is determined by a random process. Unlike the case of the Light Water Reactor (LWR) where a particular fuel element has a fixed location during each cycle and the fuel manager can shuffle fuel to optimize performance and reliability, the pebble-bed fueling scheme lacks this flexibility. Thus, while from a reliability standpoint it may be advantageous to arrange the exposure such that a fuel element sees a decreasing power density with increased burnup, this is not possible for the pebble-bed reactor. A realistic assessment of pebble-bed fuel reliability thus requires that a fuel performance model be able to accommodate such a fuel management scheme. The TIMCOAT model is capable of analyzing constant power irradiation histories, non-constant power histories, and arbitrary power histories representative of the pebble-bed fueling scheme. In the case of the pebble-bed fueling scheme the model must have realistic power and neutron flux distributions. For this analysis these distributions were obtained by running the VSOP code which was developed in Germany for the pebble-bed system [9]. The VSOP code provides power and neutron flux distributions as a function of both time and position (both axial and radial) within the pebble-bed core. A pebble (hence a particular fuel particle) is randomly re-circulated through the reactor core for the appropriate number of cycles, tracing streamlines determined by the random entry point, thus generating a unique power history for the pebble. At the same time, variables such as neutron flux, power density and coolant temperature are accumulated. Figure 12 shows a schematic of the VSOP model for the reactor. The fuel portion of the model is divided into 5 “channels” each of which is segmented into 9 or 10 “blocks”. Each block is divided into 11 “batches”. The batches within a block have approximately the same volume of fuel + gas space. The burnup is constant within a batch. The steady state core will then consist of a series of blocks within a channel where the burnup distribution as defined by the burnups in the individual batch is defined. The burnup distribution accounts for the fact that individual pebbles in a block may have been through the core a different number of cycles. VSOP provides power peaking factors down to the batch level. Figure 13 shows a typical distribution of peaking factors for a 250 MWth equilibrium core. Within a stationary block (containing 11 batches) there will be 11 volumes of fuel + gas space, each with a specific average burnup and each with an individual power peaking factor. To obtain the local power within a block, for a given batch of fuel, it is necessary to multiply the core average power by the peaking factor for that batch. To obtain the actual power density for a pebble within a batch (corresponding to a particular burnup) the packing fraction of the pebbles must be taken into consideration. This number is typically about 0.7 in the ideal case but closer to 0.6 in real cases.

Figure 14 shows a typical power history and temperature history for a highly rated fuel particle. As Figure 14 illustrates, the peak power in the particle, while generally decreasing with cycle number due to a reduction in fissionable material, is exposed to a number of cycles where the fuel is “driven” by fresh fuel in the batch. Also, while the average temperature is a generally decreasing function of time, there are cycles where the fuel temperature does not follow this general trend. Such behavior is fundamentally different than what would be the case for a stationary fuel system in a prismatic core and will have a significant effect on fuel reliability.

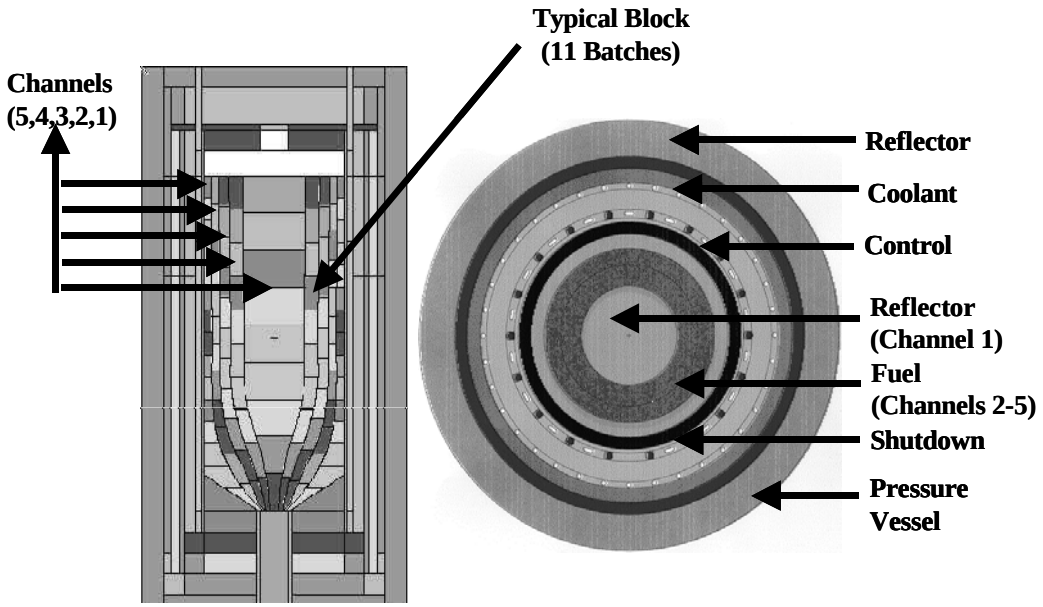

FIGURE 12. VSOP Model of a typical MPBR core.

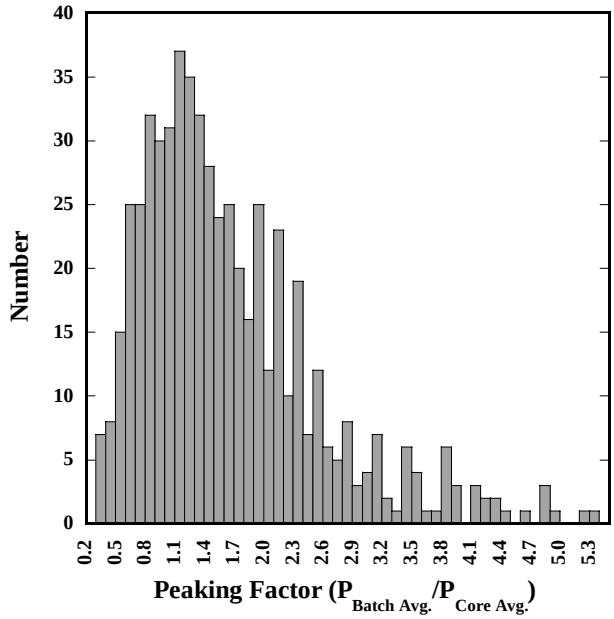

FIGURE 13. Peaking factor distribution for a typical MPBR core.

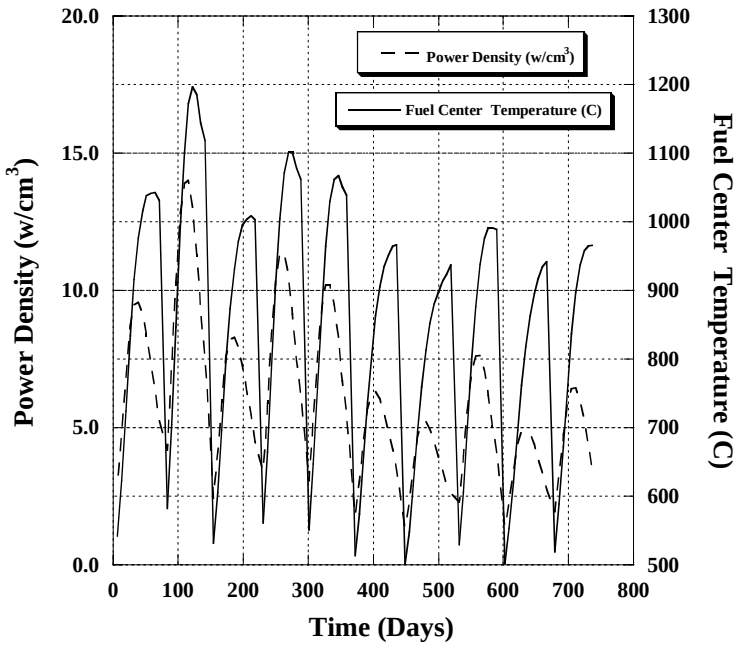

FIGURE 14. Power density vs. time for typical highly rated particle fuel subjected to a typical pebble-bed reactor power history and fueling scheme.

2.7 MONTE CARLO SAMPLING

As has been discussed above, the generation of appropriate power histories for the fuel requires that fuel pebbles be randomly added at the top of the core for each pass through the bed. In fact, what we are most interested in is the probability of failure for the fuel. Possibly the most controversial aspect of the pebble-bed concept is the contention that the fuel is sufficiently robust to eliminate the need for a containment as it is currently defined for the LWR system. It is argued that the SiC (or ZrC) barrier layer acts as one of the primary boundaries to the release of fission products during an accident. For the SiC layer to serve this purpose the failure probability, among other requirements, must be less than a value on the order of 1 part in 10^6. In the case of LWR fuel it is possible to inspect each fuel pellet to insure that fabrication requirements (enrichment, dimensions, density, etc.) are met. In the case of the pebble-bed fuel the total fuel load will contain approximately 360,000 pebbles, each containing about 11,000 fuel particles for a total of approximately 5 x 10^9 particles. For a prismatic core roughly the same number of fuel particles will be required for the same total power. While the outside dimensions of the particles can be checked, the individual layer thickness values, particle diameter, and layer mechanical and physical properties cannot be individually verified. Complete inspection requires that the particle be destroyed. For this reason, the dimensional data for actual particles will consist of: (1) a distribution of outside diameter values that have been determined by a go, no-go test to insure that the particle outside diameters are between the specified limits and (2) a set of layer dimensional distributions that will have been determined by inspecting a selected number of particles destructively. Due to the statistical nature of the pebble-bed fueling scheme and the nature of the as-fabricated data for the fuel particles, the estimation of fuel failure probability requires that a statistically significant number of “typical” fuel particles be examined. As a practical matter, this means that at least a million individual particle power histories must be examined for

which individual particle properties (dimensions and physical and mechanical) have been assigned by sampling from the property distributions. The modeler, then, is faced with determining (or estimating) the distributions associated with fuel dimensions and, physical and mechanical properties. Table 3 shows typical fuel dimensions along with estimates of either the total possible range of a property or an estimate of the standard deviation in that property [17,21,22,23]. Since much of the uncertainty in the data will be estimates unless actual data can be obtained, it will be necessary to decide the type of distribution to use for a particular property. The chosen distribution is then used to generate a cumulative probability function from which a normalized property distribution can be derived. It is the normalized distribution that serves as the basis for the Monte Carlo sampling process. As Table 3 indicates, a number of the distributions have been chosen to be piecewise linear-in this case triangular. The choice of finite distributions for a property or characteristic reflects the fact that, in many-indeed most real life-cases, it is physically impossible for a property or physical characteristic to be outside of some finite range. If one simply assumes that a property distribution is characterized by an unbounded distribution such as the Gaussian, then there is a finite probability that the Monte Carlo sampling process will result in a variable being chosen which is clearly beyond reason and that this choice will then subsequently influence the performance of a particle in a way which will influence the overall failure probability. Since we are interested in failure probabilities in the range 10^{-6}, the influence of a single non-physical result in a million cases can have a significant impact. For this reason, it is important that physically reasonable, finite distributions be chosen for properties when justified. The triangular distribution is both simple and very close to the normal distribution (Gaussian) in terms of data scattering coverage within two standard deviations. A better distribution, i.e. truncated normalized normal distribution, could be used later as a refinement of the overall model.

3.0 RESULTS & DISCUSSION

3.1 MODEL BENCHMARKING

Fuel performance models for particle fuel, such as the TIMCOAT model and others, suffer from the disadvantage that it is impossible to verify, using actual data, the detailed stresses and dimensional changes that occur in an individual particle during irradiation. Typical fuel irradiation experiments consist of several hundreds (thousands in some cases) of individual fuel particles being fabricated into a fuel compact. The compact is then irradiated. Data collected during the irradiation include only average temperatures and fission gas release rates. It is impossible to narrow the measurement down to the individual particle level. The fission product release data is sufficiently precise as to allow the determination of a single particle failure, but post irradiation examinations are not capable of locating the actual particle (except by chance) that failed within the compact. Thus, we are left with the outcome that the results of the calculations cannot be verified to a level that is normally accomplished for LWR fuel irradiations. Moreover, the only actual data points are the indications, through release/birth (R/B) measurements for fission gas (normally Kr) that a particle has failed. Local temperatures and power histories are available for test capsule irradiations but actual particle temperatures are not. Absent actual fuel-specific data such as temperature and layer stresses, we have chosen a three-tier approach to the establishment of the voracity of our model: (1) to compare our model stress calculations with finite element calculations, (2) to compare our results with those of other fuel performance models when it comes to fuel temperature distributions, stress calculations and other fuel-related variables and, (3) to compare our model results to fuel failure probability with data from capsule irradiations where possible. With respect to a comparison with finite element calculated stresses, we compare our model results with finite element results from INEEL for identical particle dimensions and thermal and fluence history. With respect to comparisons with other fuel performance models, we compare our results with those of a fuel performance model developed by Sawa et al. [24]. With respect to comparison of results for fuel failure probability we compare our model results with experimental data from New Production Reactor (NPR) fuel development irradiations, in particular capsules NPR1 (A1-A8), NPR2-A4, and NPR1A-A9 [5].

Table 3.

NPR Fuel Particle Properties & Distribution Parameters

Property	Mean Value	Std. Dev.	Dist. Type
Kernel Diameter (μm)	200	5.2	Triangular
Buffer Thickness (μm)	102	10.2	Triangular
IPyC Thickness (μm)	53	3.68	Triangular
SiC Thickness (μm)	35	3.12	Triangular
OPyC Thickness (μm)	39	4.01	Triangular
Fuel Density (gm/cm^3)	10.51	0.01	Triangular
Buffer Density (gm/cm^3)	0.93	0.05	Triangular
IPyC Density (gm/cm^3)	1.923	NA**	NA
OPyC Density (gm/cm^3)	1.855	NA	NA
IPyC Characteristic Strength (MPa)	23.6* (MPa-m$^{3/\beta}$) [17]	9.5 (modulus,β)	Weibull
OPyC Characteristic Strength	22.4* (MPa-m$^{3/\beta}$) [17]	9.5 (modulus,β)	Weibull
SiC Characteristic Strength	9.64 (MPa-m$^{3/\beta}$) [17]	6.0 (modulus,β)	Weibull
SiC K_{IC} (MPa√m)	3300 [23] Triangular		530
IPyC BAF_0	1.05788 Triangular		0.00543
OPyC BAF_0	1.05154 Triangular		0.00622

* The characteristic strength of PyC is dependent on its BAF_0: $\sigma_0=154.46*BAF_0^2-141.1*BAF_0$ [17]
** Not Available

3.1.1 STRESS COMPARISON

Figure 15 shows the results of a comparison between the TIMCOAT model and the results, for identical initial particle dimensions and material properties, of finite element based calculations performed at INEEL. The case data are presented in Table 4. The plot is for the evolution of the tangential stress at the inner surface of the IPyC layer as a function of fluence. Both the TIMCOAT model and the model being developed at INEEL use the same data set for pyrocarbon shrinkage and swelling but use different interpolation methods to obtain values for strain states not explicitly present in the data base [17]. The comparison temperature was chosen to coincide with a temperature for which interpolation would be minimal to reduce errors from this source. In order to illustrate the effect of varying Poisson's ratio in irradiation creep for pyrocarbon, we also show TIMCOAT results using both a fixed Poisson's ratio of 0.5 as well as varying values essentially according to Fig. 9. In the actual TIMCOAT model we allow it linearly decrease from 0.5 to 0.4 until the effective octahedral shear creep strain reaches 0.01 after which it remains constant at 0.4. As the comparison shows, the two methods produce very similar results both in terms of the general trend and the peak stress achieved. A small deviation in the time for peak stress was observed and was traced to differences in the interpolation scheme used for strain in the pyrocarbon. It is also shown that allowing the Poisson's ratio in irradiation creep for pyrocarbon to change may have a

significant influence on particle stress predictions and, as a result, fuel performance predictions. In this case stresses differ by about 90MPa. As a result of this behavior, and assuming that the effect is in accordance with the data, this phenomenon should not be overlooked by modeling efforts.

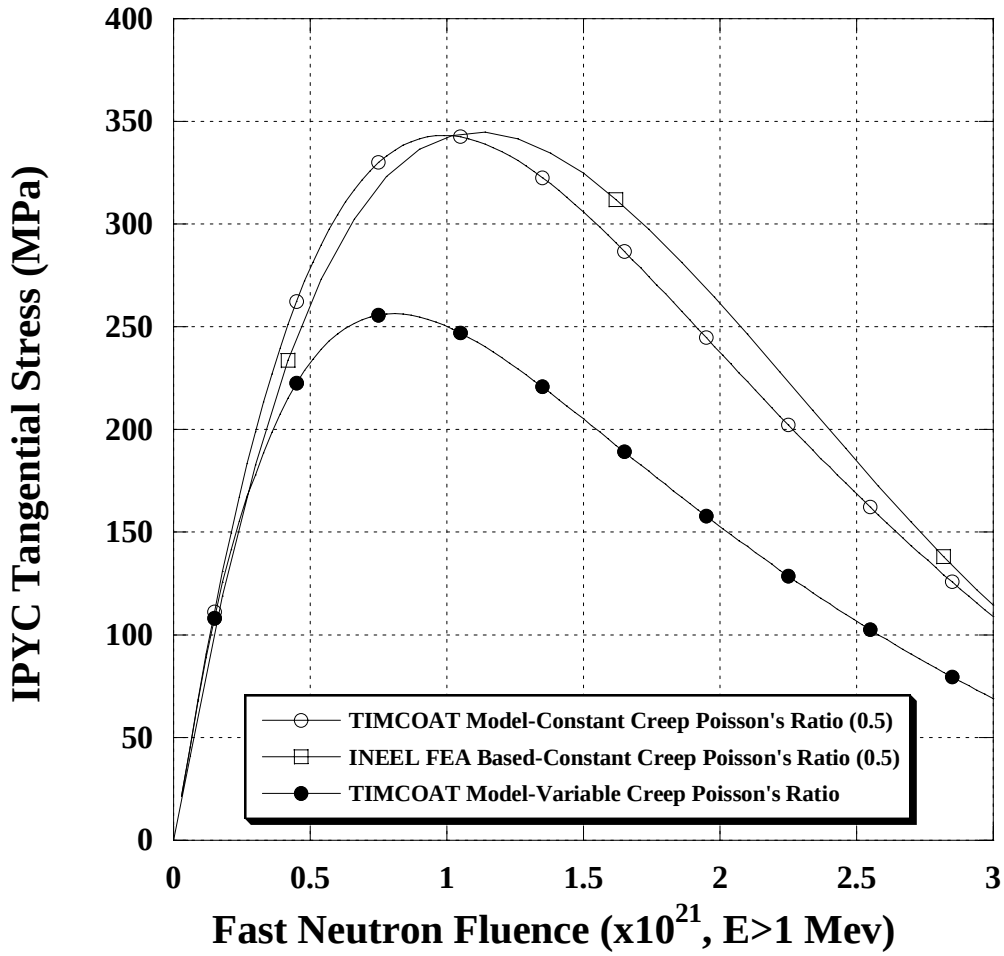

FIGURE 15 Comparison of TIMCOAT and INEEL calculated IPyC tangential stress evolution with fluence. Conditions: (1) Isotropic pyrocarbon properties, Poisson's ratio in creep = 0.5, BAF_0=1.0; (2) density 1.96 gm/cm^3; (3) constant irradiation temperature of 1032°C.

3.1.2 COMPARISON WITH SAWA ET AL. RESULTS

Sawa et al. have reported results of a model that has been developed in Japan and applied to the performance of High Temperature Test Reactor (HTTR) initial fuel loading [24]. The HTTR uses particle fuel arranged in a prismatic core design. The key parameters for this analysis are given in Table 5. In the comparison, we used the properties given by Sawa et al. where possible. However some of the properties were not provided in their paper. In such cases a best estimate engineering judgment was made as to the appropriate properties to use. The mechanical properties and irradiation data for pyrocarbon and SiC were not provided and so were taken from Ho [17]. The fuel particles were irradiated to $3.0\times10^{21} cm^{-2}$ at a temperature of 1300°C. The results of this comparison are shown in Figure 16.

Table 4.

The Benchmarking Case for Stress Comparisons between MIT and INEEL predictions

Property	Mean Value
Kernel Diameter (μm)	200
Fuel Density (gm/m^3)	10.52
Buffer Thickness (μm)	102
Buffer Density (gm/cm^3)	0.9577
IPyC Thickness (μm)	53
IPyC Density(gm/cm^3)	1.96
SiC Thickness (μm)	35
OPyC Thickness (μm)	39
OPyC Density (gm/cm^3)	1.96
IPyC/OPyC BAF_0	1.0
Fuel Temperature (°C)	1032
EOL Fast Fluence (E>0.18 MeV)	3.0 x 10^{21} (n/cm^2)
EOL Burnup (%FIMA)	70
Ambient Pressure (MPa)	6.38
Fuel Type	UCO
C to U ratio	0.36
O to U ratio	1.51
U235 Enrichment (%)	93.15

In Figure 16, the lines with open symbols represent TIMCOAT model calculations of tangential stresses in each structural layer. The lines with filled symbols are from Sawa et al. Initially, the SiC is placed in compression due to neutron-induced shrinkage of the adjacent PyC layers. Accordingly, the IPyC and OPyC layers are in placed in tension. As the irradiation progresses, the pyrocarbon shrinkage rate gradually decreases, but only slightly. At the same time, fission gas builds up in the buffer layer which results in an increase in the internal pressure and, hence, drives the layer stress in the positive direction. The internal pressure buildup eventually offsets the shrinkage induced compression in the SiC and leads to increasing tensile stress at the end of the exposure. At higher fluence the stress is dominated by the internal pressure in the particle. The model calculations for the SiC layer agree with each other quite well at high burnup, whereas our results show a slower relaxation early in the irradiation. The calculations from Sawa et al. exhibit an abrupt change at a fluence of 0.1 x 10^{21} cm^{-2}. Their calculations show approximately linear behavior afterwards. In fact, the results of Sawa show two linear regions of behavior. However, experimental data for PyC shrinkage is not this abrupt and is unlikely to induce stresses such as these. It is likely that the Sawa et al. model uses a more simplified PyC shrinkage and/or creep model and their stress analysis is more approximate than ours. The discrepancy between two stress predictions in the pyrocarbon layers is probably due to the use of different mechanical properties for pyrocarbon. For example, the PyC layers appear to be more rigid in Sawa's results than in ours. Nevertheless, the stress evolution in the pyrocarbon layers follows the same trend.

An estimation of the HTTR fuel failure probability was obtained through a Monte Carlo analysis that sampled 1,000,000 particles. In this comparison the layer thickness and densities were sampled using a normal distribution with standard deviations as indicated in Table 5. The fracture strength of the PyC and SiC layers were described by Weibull distributions, the parameters of which are also listed in Table 5. The cumulative Weibull function is defined as

$$C_W(\sigma_f) = 1 - \exp\left[-\left(\frac{\sigma_f}{\sigma_{f0}}\right)^{\beta}\right], \tag{41}$$

where σ_{f0} is the mean fracture strength of a particular layer and β is the Weibull modulus. From Equation (41), we can express the fracture strength σ_f in terms of C_W,

$$\sigma_f = \sigma_{f0} \exp\left\{\ln\left[-\ln\left(1 - C_W\right)\right] / \beta\right\}. \tag{42}$$

It can be shown that σ_f follows the Weibull distribution if C_W is randomly sampled between 0 and 1 [25]. To compare with the results of Sawa et. al, the dependence of SiC layer mean strength on neutron fluence is assumed to follow the relationship suggested in his paper [24].

$$\sigma_{f0} = 834 - 88 \times \Phi t \tag{43}$$

where Φ_t is the neutron fluence in units of 10^{21} n/cm^2. Using the above data, the TIMCOAT model predicts a failure probability of approximately 16% for HTTR fuel. Failure is predicted to be due, in all cases, to pure pressure vessel failure. These results are in good agreement with the Sawa et al. prediction [24].

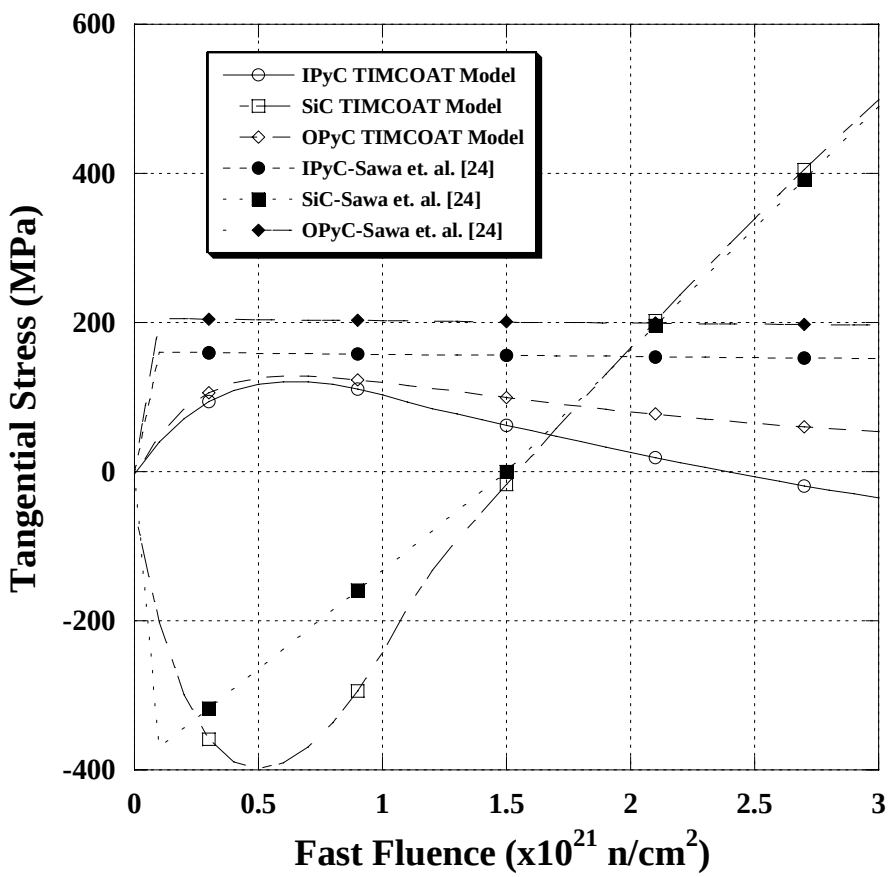

FIGURE 16. Comparison between the TIMCOAT model and the results of Sawa et al. for behavior of HTTR fuel.

Table 5

HTTR Fuel Characteristics

Property	Mean Value	Std. Dev.	Distribution Type
Kernel Diameter (μm)	600*	12.0	Gausian
Fuel Density (gm/m^3)	10.7	0.1	Gausian
Buffer Thickness (μm)	60*	10.0	Gausian
IPyC Thickness (μm)	30*	6.0	Gausian
IPyC Density(gm/cm^3)	1.96		
SiC Thickness (μm)	25*	2.0	Gausian
OPyC Thickness (μm)	45*	3.0	Gausian
OPyC Density (gm/cm^3)	1.81		
Buffer Density (gm/cm^3)	1.1*		
IPyC/OPyC BAF_0**	1.02		
Fuel Temperature (°C)	1300*		
Fast Fluence (E>0.18 MeV)	3.0 x 10^{21} (n/cm^2)*		
UO_2 Enrichment (% U-235)	9.17		
EOL Burnup (GWd/T)	66*		
IPyC/OPyC Strength (MPa)	160*	4.0 (modulus)*	Weibull [24]
Initial SiC Strength (MPa)	834*	8.0 (modulus)*	Weibull [24]
SiC K_{IC} (MPa√m)	3300 [23]	530	Triangular

* Values that given by K. Sawa, et al. [24]; chosen by authors if not noted.
** Bacon Anisotropy Factor

3.1.3 COMPARISON WITH NPR CAPSULE IRRADIATIONS

As a part of the New Production-Modular High Temperature Gas Reactor (NP-MHTGR) program, an extensive particle fuel and irradiation program was conducted [5]. As a part of this irradiation program several capsules were irradiated. Among these were capsules NPR1, NPR2, and NPR1A. NPR1 and 2 were irradiated in the high flux isotope reactor (HFIR) while capsule NPR1A was irradiated in the advanced test reactor (ATR) [5]. The NPR1 and NPR1A irradiations were designed to expose fuel to maximum temperature, burnup and fluence while the NPR2 irradiation was designed to expose fuel to high burnup and fluence, but at lower temperatures. A detailed description of the capsules is provided in References [5] and [26]. The NPR1 and 2 capsules each contained 16 compacts, numbered A1 to A8 and B1 to B8, which, in turn, each contained several thousand particles. The A1-A8 compacts were essentially the same as the B1-B8 compacts in terms of the fuel itself and irradiation conditions. For example, compact A1 was opposite compact B1 at the same level in the NPR1 and 2 capsules. For this reason it was assumed that only one of the groups (A or B) need be simulated. The NPR1A capsule contained 20 compacts, each containing several thousand particles. A total of 221,136 particles were irradiated. Of these approximately 700 failed. Table 6 shows the key features and results of these irradiations. At the time of these irradiations it was believed that the particles had been fabricated using the best technology available and that fuel failure should not occur. Moreover, fuel performance models developed specifically for these programs predicted that no failures should occur [5]. None the less, failures did occur. A significant post irradiation examination (PIE) program was conducted to evaluate the cause of failure and, based on these results, an even more significant PIE program was planned. However, the program was canceled before this second campaign could be carried out. The results of the initial PIE program showed that, contrary to the performance of German fuel, the NPR fuel showed extensive

pyrocarbon layer cracking followed by, in some cases, cracking of the SiC layer. In some cases the number of particles with IPyC cracking exceeded 60%. Recent detailed analysis of the NPR irradiations conducted by the INEEL indicate that the failures were driven by shrinkage of the pyrocarbon due to a higher than expected degree of anisotropy [27]. The cause of this unexpected anisotropy, proposed by the INEEL scientists, was the lower deposition rate for the pyrocarbon layers that is commonly used by German fabricators. While the INEEL analysis may indeed be an accurate one, modeling efforts need to be conducted to confirm this qualitative analysis, and the possibility exists that some other variable(s) may be at work in the process. An indication that this may be the case can be seen in the "anomalous" behavior of compact NPR1-A8 which had a far lower failure rate than would have been expected based on its placement in the irradiation train and the failure rate of companion compacts but was fabricated using the same fuel and in the same manner as the other capsules. One reason could be that NPR1-A8 was at the end of the fuel stack during irradiation in HFIR and probably saw a wide variation of neutronic conditions across the compact, due to the sharp axial cosine profile of the flux. While this behavior could also have been caused by an unknown deviation in material properties, this has been discounted based on extensive quality control exercised during fabrication. Nevertheless, there is the likelihood that the irradiation history may have played a key role and that the models of the day did not accurately represent the physics of the system. The TIMCOAT model has been formulated using as accurate a physics model as possible based on the knowledge of particle fuel behavior and the availability of data, including accounting for the anisotropy of irradiation induced dimensional change of pyrocarbon, the dependence of Poisson's ratio in irradiation creep, and incorporating an advanced failure model which incorporates a cracking model which has, it is argued, a better chance of accounting for, and taking into consideration the observed failure mode for the NPR fuel. Furthermore, the TIMCOAT model can deal with arbitrary irradiation histories, so that detailed irradiation experiments can be simulated.

Table 6

Simplified History Irradiation Conditions for NPR compacts

Compact ID	Fast Fluence (10^{25} n/m^2)	Irradiation Temp. (°C)*	Burnup (% FIMA)
NPR1-A1	2.4	874	74.0
NPR1-A2	3.0	1050	77.0
NPR1-A3	3.5	1036	78.5
NPR1-A4	3.8	993	79.0
NPR1-A5	3.8	987	79.0
NPR1-A6	3.5	1001	78.5
NPR1-A7	3.0	1003	77.0
NPR1-A8	2.4	845	72.0
NPR2-A4	3.8	746	79.0
NPR1A-A9	1.9	1052	64.0

* Time Averaged Temperature

3.1.3.1 GENERAL CHARACTERISTICS OF THE NPR IRRADIATIONS

The NPR capsules each contained a series of compacts, as described above. As Table 6 shows, the NPR1 capsule was irradiated at a higher capsule average temperature than the NPR2 capsule. This was the only nominal difference between these capsules. The NPR1A capsule was irradiated at the same capsule-average temperature as that of NPR1 but to a lower fluence and burnup. Thus, to a first approximation, the behavior of NPR1 and 1A should have been similar at the EOL burnup of NPR1A. However, upon closer examination, it is clear that the irradiation history of NPR1, 2 and NPR1A were very different in

terms of the rates of accumulated fluence and burnup. Figures 17 and 18 show temperature, fluence and burnup histories for the compacts NPR1-A5, NPR1-A8, NPR2-A4, and NPR1A-A9. Also shown in Figure 17 is the constant, time averaged, temperature for each of the compacts. Except for compact NPR1-A8, these compacts resided at comparable, center, locations within there respective capsules. The NPR1A capsule experienced an approximately constant accumulation rate of both burnup and fluence and the ratio of burnup to fluence was approximately constant during exposure. The NPR1 and 2 capsules, on the other hand, experienced a very different burnup and fluence accumulation history. These capsules experienced a very large increase in burnup during the first 50 full power days of exposure-approximately 50% of the target burnup-while achieving only 6% of the target fluence. The reason for this difference was the fact that the NPR1 and 2 capsules were irradiated in two different locations within the HFIR while the NPR1A capsule was irradiated in a single location in the ATR. Since it is the fluence-temperature that drives the behavior of pyrocarbon swelling and creep we would expect very different behavior of the stress evolution for these two exposure histories. We would also expect different cumulative creep and swelling effects for capsules irradiated at constant temperature and capsules which experienced variable temperature histories. These effects should result in different pyrocarbon cracking behavior for the two cases. Figure 19 shows the entire temperature history set for the NPR1 capsule compacts and illustrates the range of temperatures that individual compacts experienced.

As figures 17-19 indicate, the compact temperatures were variable during the irradiation in spite of efforts to tailor the designs, altering the thermal resistance of the system during exposure, to minimize this. Also, since it was impossible to measure the exact temperatures within a compact, a model of the overall system was used to calculate these temperatures. This introduced a considerable amount of uncertainty in these temperatures although the relative differences between individual compacts would have been maintained during exposure. Figures 23 and 26 show the effect of this uncertainty on the "nominal" temperature histories for compacts NPR1-A8 and NPR2-A4. These figures also illustrate another characteristic of the irradiations. While the NPR1 and NPR2 irradiations were conducted in the same facility the shape of the temperature-time histories were significantly different. The NPR1 compacts experienced an approximately constant average temperature. The NPR2 capsules experienced a generally decreasing average temperature for the first 100 full power days followed by a jump in average temperature for the last 75 full power days of irradiation. With respect to the detection of particle failure, the Kr^{85m} R/B was measured only for the entire capsule-not for individual compacts within the capsule. There was adequate sensitivity for: (1) the detection of individual particle failures, (2) the point of first failure, (3) and the approximate rate of subsequent failures. However, the isolation of a particular failure to a specific compact could not be determined. Moreover, PIE of the order of only 100 particles within each compact was used to estimate the total failure fraction within each compact. The combination of a small number of particles examined per compact with only global sensitivity for failure indication resulted in considerable uncertainty in the reported failure probability [5].

For this comparison we analyzed the NPR1, 2 and 1A capsules, but focused on the NPR-1 capsule in particular. For the NPR2 capsule we analyzed the behavior of compact A4. For capsule NPR1A we focused on compact A9. These capsules were part of the PIE analysis. In the case of capsule NPR1 we analyzed all of the compacts, A1-A8 (B1-B8 are equivalent to A1-A8 as described above). The NPR1A and 2 comparisons allowed only a comparison of ultimate failure probabilities while the NPR1 comparison allowed both a comparison of failure probabilities and a comparison of the time of failures as indicated by Kr^{85m} R/B. However, it should be noted that even for capsule NPR1, the exact relationship between an individual particle failure and its location could not be made since it is impossible to connect a particle failure to a location in the experimental data.

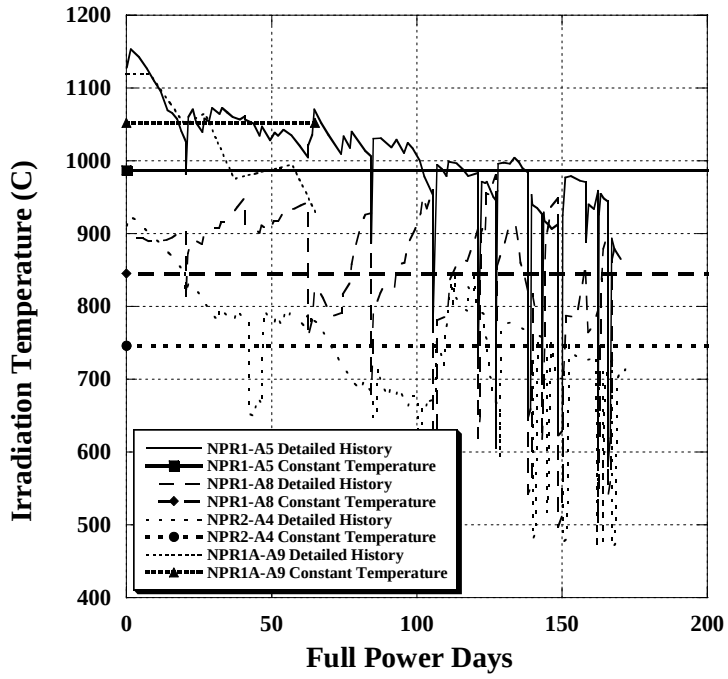

FIGURE 17. Temperature histories for NPR1-A5, NPR1-A8, NPR2-A4 and NPR1A-A9 compacts.

3.1.3.2 COMPARISON PROCEDURE

For this analysis we modeled the fuel system at two levels of detail with respect to the irradiation histories of the capsules: (1) based on a simplified temperature history, and (2) based on a detailed representation of the temperature history. For the simplified comparison we assumed that the exposures took place at a single average temperature. Table 3 shows the irradiation conditions for the constant temperature irradiation histories. These temperatures were obtained from Reference [26]. A second, more detailed analysis was performed using as accurate as possible irradiation histories for each compact. These histories were manually extracted from the detailed capsule irradiation report [26]. Figure 17 shows the detailed history, with the level of the constant temperature history identified, for the compacts for which PIE was performed. Figure 19 shows the detailed histories for all of the compacts in NPR1. For each comparison a Monte Carlo simulation was performed using a million particles as the basis for each case. Table 3 shows the characteristics of the input distributions for the particle properties. As was discussed earlier, triangular distributions were used for fuel characteristics based on the assumption that for actual engineering systems there are physical limits for both properties and dimensions. Some engineering judgment was used in determining the limits on the distributions but we attempted to be consistent and to maintain the width at half maximum in the triangular distributions equal to that for an “equivalent” Gaussian distribution with the same standard deviation.

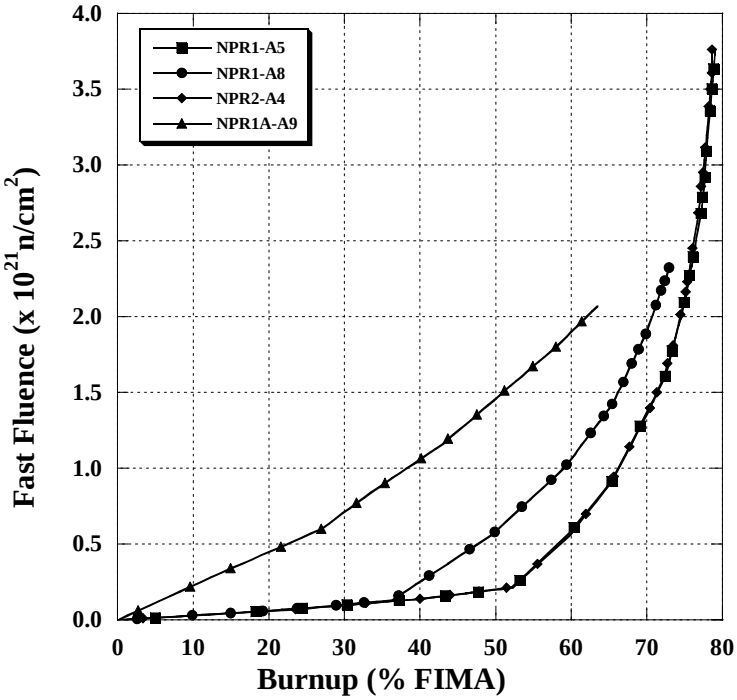

FIGURE 18. Fluence vs. burnup for compacts NPR1-A5, NPR1-A8, NPR2-A4 and NPR1A-A9.

3.2 RESULTS & DISCUSSION-NPR COMPARISON

Tables 6-9 show irradiation conditions (Table 6) and the overall results for the analysis. Figures 20-32 show more of the details of the results. Please note that the symbols in these figures are not meant to represent actual data points, but are added to the plots for clarity. Tables 7 and 8 show the results for the IPyC and SiC (particle) failure probabilities including a comparison between model predictions and actual data. In general, the TIMCOAT model does a very credible job overall for both the IPyC and particle failure probabilities. Half of the predictions are well within the uncertainty bands for the actual performance. Given the complexity of the non-linear interaction between temperature, stress, and creep rate, this should not be surprising. There are, however, significant deviations for some of the capsules. In particular, the IPyC failure rates for NPR1-A8 and NPR2-A4 are significantly different than the actual data. Also, the particle failure prediction for NPR2-A4 is significantly different than the actual value. Possible reasons for this behavior will be discussed below. Figure 20 shows a plot of the Kr^{85} R/B and cumulative failure fraction vs. full power days for the entire NPR1 capsule. Table 9 presents the key results in tabular form for the NPR1 capsule. The predicted Kr^{85} R/B is obtained by multiplying the number of failed particles at the time by 1.7×10^{-7}, which is the release of one failed particle [5]. The overall predicted failure probability for the capsule using detailed irradiation histories compares very favorably with the actual value (0.846% vs. 0.806%). The shape of the calculated Kr^{85} R/B curve also compares very favorably with the actual data. The point of initial particle failure is significantly earlier than the actual behavior. The probable reason is that in this version of crack-induced fuel failure model,

the SiC layer is either instantaneously failed by PyC cracking or stays intact unless pressure vessel failure occurs later on, but the real scenario may be that there is some delay of SiC failure after IPyC failure. However, it should be noted that the predicted point of initial failure compares much more favorably for the detailed history than for the constant temperature history.

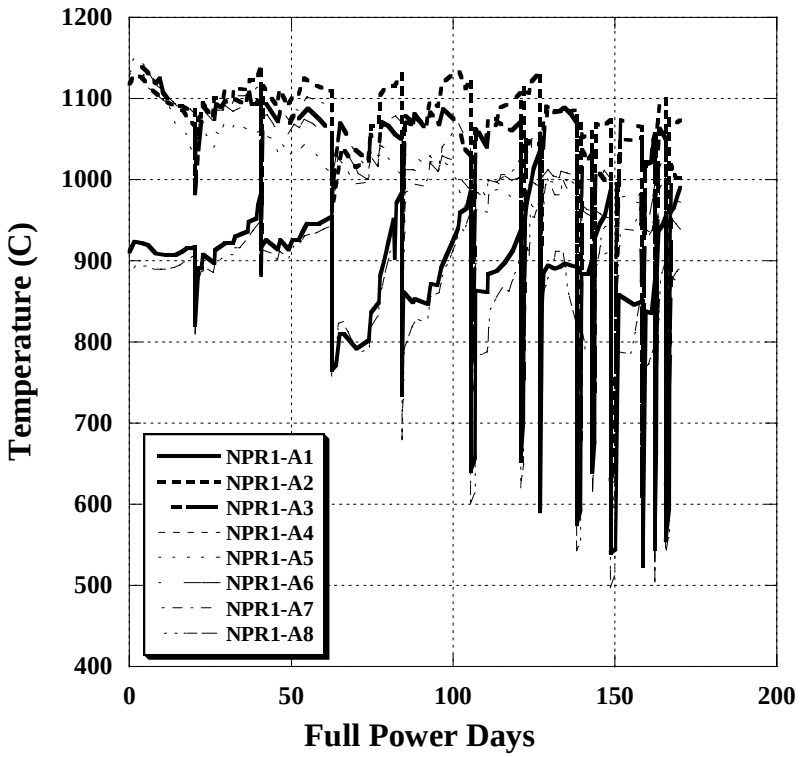

Figure 19. Temperature histories for NPR1 compacts.

For purposes of further discussion we will focus on the results for the compacts for which PIE data was obtained. Figures 21-30 present detailed results for each of these compacts. Figures 21 and 22 show detailed results for compact NPR1-A5. Figures 23-25 show detailed results for compact NPR1-A8. Included in these results is the effect of uncertainty in temperature in the overall failure prediction. For the temperature uncertainty comparison it was assumed that the temperature at a given point in the power history was either at the upper 95% limit of the predicted exposure temperature range or at the lower 95% limit for the exposure temperature. The purpose of this investigation was to determine if the overall model failure probability could be dominated by the uncertainty in temperature during an irradiation-negating the difference between using the detailed temperature history as opposed to assuming a constant temperature exposure. Figure 23 shows a plot of the resulting set of temperature histories. Figures 24 and 25 show the resulting spread in IPyC and particle performance. The assumption of a constant deviation in temperature during an irradiation is a severe one. In spite of this, the results show that the resulting uncertainty in failure probability due to temperature uncertainty is less than the uncertainty introduced by assuming that exposure occurs at a constant temperature. Figures 26-28 show the detailed results for compact NPR2-A4. Once again, the effect of temperature uncertainty is explored. Figure 26 shows the temperature history for

the nominal, upper 95% and lower 95% cases. When the results of this compact are compared with the NPR1-A8 cases, the effect of exposure temperature and temperature shape becomes apparent. The deviation in predicted results is much narrower for these cases. This is a result of a much smaller deviation in stress history between the detailed and simple temperature histories for this compact. This will be further discussed below. Figures 29 and 30 show the detailed results for compact NPR1A-A9. There is a significant difference between the detailed and constant temperature histories.

Table 7
Comparison of Model Calculations with PIE Results for NPR compacts

IPyC Layer Results

Compact ID	% Failed History(%)	95% Confidence	Detailed History (%)	Simple
NPR1-A1	NM*	-	47.4	84.2
NPR1-A2	NM	-	6.44	16.7
NPR1-A3	NM	-	15.0	19.4
NPR1-A4	NM	-	33.5	33.9
NPR1-A5	31	17<p**<47	26.6	36.3
NPR1-A6	NM	-	24.4	30.3
NPR1-A7	NM	-	15.6	29.1
NPR1-A8	6	2<p<16	60.7	91.7
NPR2-A4	65	54<p<76	99.6	99.5
NPR1A-A9	18	5<p<42	23.9	19.0

* Not Measured
** failure probability

Table 8
Comparison of Model Calculations with PIE Results for NPR compacts

SiC (Particle) Failure Results

Compact ID (%)	% Failed	95% Confidence	Detailed History (%)	Simple History
NPR1-A1	NM*	-	1.61	8.32
NPR1-A2	NM	-	1.0×10^{-4}	0.0380
NPR1-A3	NM	-	0.025	0.0740
NPR1-A4	NM	-	0.857	0.613
NPR1-A5	0.6	0<p<3	0.358	0.790
NPR1-A6	NM	-	0.272	0.400
NPR1-A7	NM	-	0.0683	0.337
NPR1-A8	0	0<p<2	2.74	9.64
NPR2-A4	3	2<p<6	13.9	12.8
NPR1A-A9	1	0<p<5	0.492	0.075

* Not Measured
** failure probability

Table 9

Overall Statistics for Capsule NPR1

Item	Actual	Prediction Detailed History	Prediction Simple History
# Particles	77,500	77,500	77,500
# Failed Particles	625	656	2384
Failure Probability	0.806%	0.846%	3.076%
Peak Fluence @ Initial Failure (x 10^{21} n/cm^2)	1.7	0.59	0.07
Peak Burnup @ Initial Failure (%FIMA)	72%	59%	24%
EFPD @ Initial Failure	108	74	20
Peak Temperature @ Initial Failure (°C)	1123	1025	1086

In the TIMCOAT model failure is driven by the initiation of a crack in the IPyC followed by propagation, if conditions are right, of the crack through the SiC layer. The overall process is a mechanical one. Thus, the failure process (time, stress at failure, etc.) will be governed by the balance between creep, which tends to relax stresses, and swelling, which will tend to increase stresses. The entire process will be thus governed by the response of the pyrocarbon to the neutron exposure. Internal pressure buildup will be a small contributor until high burnups when fission gas pressure becomes significant. Failure thus occurs when, upon cracking of the IPyC layer, the resulting stress intensity factor, K, is sufficient to exceed the fracture toughness, K_{IC}, of the SiC layer. Figures 31 and 32 show the evolution of stress during irradiation for the compacts for which failure data were determined. Figure 31 shows the circumferential stress evolution in both IPyC and SiC layers while Figure 32 shows a more detailed expansion of the circumferential stress calculation in IPyC layer during the period where peak stresses are achieved. Inspection of Figure 32 yields insight into why using the detailed history is important for more accurate modeling of the performance. For the case of the NPR1 compacts there is a significant deviation between the stresses calculated for the detailed and constant temperature histories. The most significant deviation is for NPR1-A8. This compact has historically been the most difficult to model and represents "anomalous" behavior in that no failed particles were found during PIE. Based on an assumption that failure fraction is roughly inversely proportional to the average temperature, the NPR1-A8 failure fraction should have been between that of NPR2-A4 (average temperature 746°C) and NPR1-A5 (average temperature 987°C). Inspection of Figure 32 shows that the stresses for the constant temperature history are significantly higher than for the detailed temperature history. Moreover, the calculated stress range for this compact overlaps the region of high sensitivity of the IPyC to fracture as well as the stress region which results in increased failure rates of the SiC. The two temperature histories, shown in Figure 17, indicate that the detailed temperature history results in a higher average temperature (than the history average) during the first 75 days of exposure. This will result in a higher average creep rate and, hence, more stress relaxation during this period. This period also corresponds to the period of maximum radial swelling as illustrated in Figure 10. The combination of a higher average temperature in the region of swelling where stress relaxation will be most important results in lower stresses and subsequent lower failure probabilities. While using the detailed temperature history is not able to explain the behavior of

NPR1-A8, using this history is definitely more realistic and, it is argued, should be employed whenever possible in evaluating fuel performance.

At the opposite end of the spectrum is compact NPR2-A4. As Figure 32 illustrates, the detailed and constant temperature power histories yield essentially the same stress vs. fluence history. Given the stress history evolution it is not surprising that the calculated failure probability results will be very similar. However, compact NPR2-A4 is also the compact which is the most poorly modeled. The predicted IPyC and particle failure probabilities are considerably higher than the actual failure probabilities-outside of the uncertainty band for the PIE results. None the less, the model predictions are consistent with this compact having the highest measured IPyC failure rate and the highest particle failure rate.
We have discussed that temperature variations have much larger effects on the stress level of NPR1-A8 than that of NPR2-A4. The main reason for this "behavior" is that the creep rate given by Eqn. 40 has a minimum at around 650 to 700°C, and for NPR2-A4 whose average irradiation temperature is 746°C, the creep rate is much less sensitive to temperature variation than in NPR1-A8 (845°C), NPR1-A5 (987°C), and NPR1A-A9 (1052°C). Also, the very detailed temperature histories will cause differences in the stress development in compacts. For example, in Figure 23, the irradiation temperature in NPR1-A8 was generally upward sloping in each cycle, whereas in Figure 26, the irradiation temperature in NPR2-A4 was generally downward sloping in each cycle.

The significance of the fluence accumulation pattern with respect to burnup can be seen by comparing the calculated failure probabilities for compacts NPR1-A2 and A3 with that for compact NPR1A-A9. Figure 18 shows the fluence accumulation for capsules NPR1 and NPR1A. The NPR1A capsule experienced a much higher rate of fluence accumulation versus burnup than the NPR1 capsule. The average EOL fluence for the NPR1 capsule was approximately 3.5 x 10^{21} n/cm^2 while the EOL fluence for the NPR1A capsule was only 1.9 x 10^{21} n/cm^2. Yet, the predicted failure probability for the NPR1A compact is approximately 20 times that of the NPR1 compacts that operated at similar average temperature (~ 1050°C: compacts NPR1-2, NPR1-3) and this higher failure probability was achieved at just under half the fluence. This difference is likely to do with the specific temperature histories for three compacts, but the interplay between the dependence of irradiation induced dimensional change and creep on fluence as shown in Figure 10 and the dependence of internal fission gas pressure on burnup also plays a role. The internal pressure offsets the tensile stress in the IPyC layer induced by shrinkage at the early stage of irradiation, because internal pressure helps to put the IPyC layer back toward its original location before shrinkage. In the case of NPR1 and NPR2, compacts gain 40% - 50% of burnup when internal pressure is already significant, whereas they only experience 0.1x10^{21} n/cm^2 of fast neutron fluence and hence only a small amount of shrinkage. This causes the resultant tensile stresses in the IPyC layer of NPR1-A2 and A3 to be lower than that of NPR1A-A9 at an early stage of irradiation, where generally tensile stress quickly builds up in the IPyC layer. The results of this analysis highlight the importance of considering the total irradiation environment during fuel testing. The NPR1 and NPR1A capsules were intended to be similar to each other-at least in exposure temperature. Given the critical dependence on fluence accumulation rate, this similarity was not achieved.

4.0 CONCLUSIONS

The TIMCOAT model represents the first model for coated particle fuel to make use of the combination of: (1) a probabilistic fracture mechanics model for failure, (2) the ability to treat variable material properties, specifically irradiation induced dimensional changes, creep and Poisson's ratio in creep as a function of irradiation conditions, and (3) the application of Monte Carlo techniques to account for materials properties as well as history variable uncertainty. The model has been benchmarked against other models as well as PIE data from the NPR irradiation program. The model aims at a better understanding of fuel particle failure mechanisms and the effect of material and history variables on fuel reliability. The results of the model compared with PIE data are encouraging.

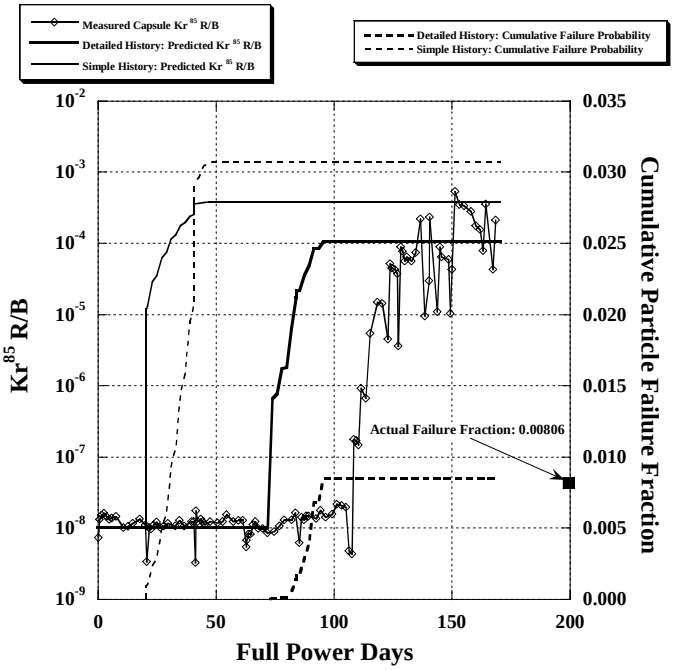

FIGURE 20. Kr^{85} R/B and cumulative failure fraction for capsule NPR1.

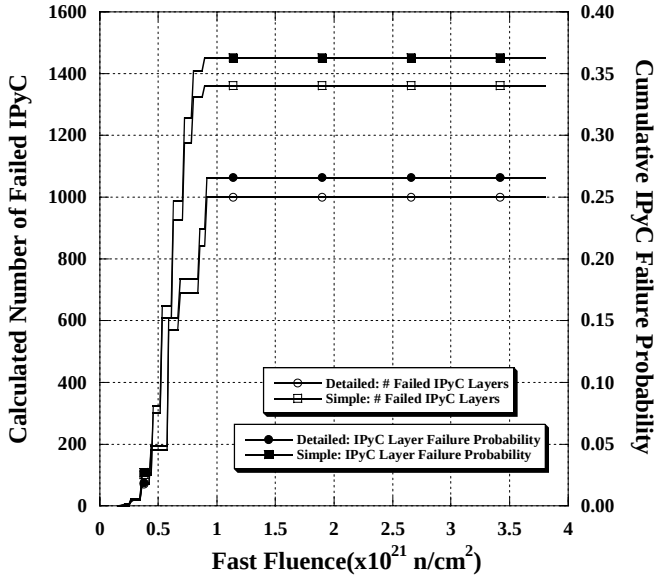

FIGURE 21. Compact NPR1-A5 IPyC calculated failure vs. fast fluence.

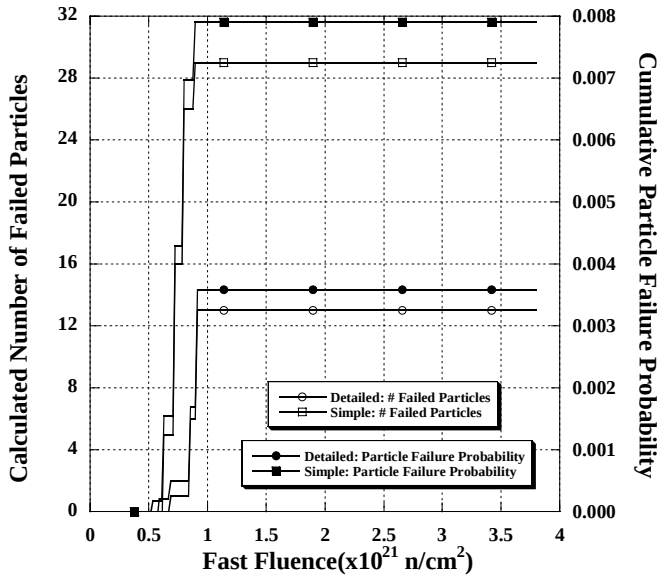

FIGURE 22. Compact NPR1-A5 calculated particle failure vs. fast fluence.

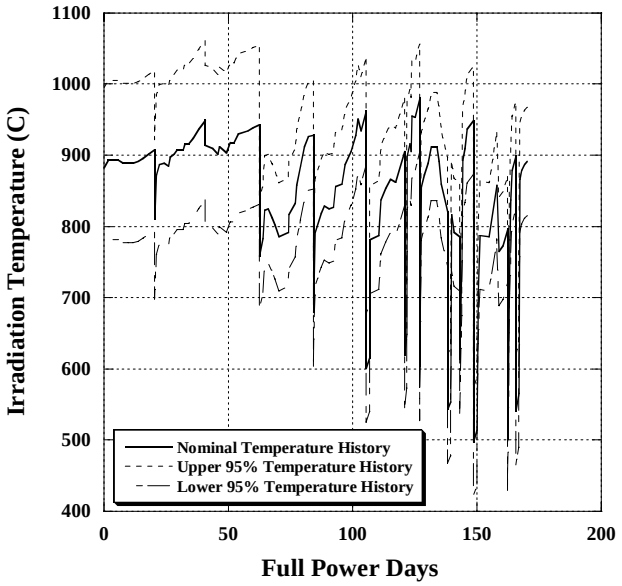

FIGURE 23. Temperature history for compact NPR1-A8 showing upper and lower 95% temperatures.

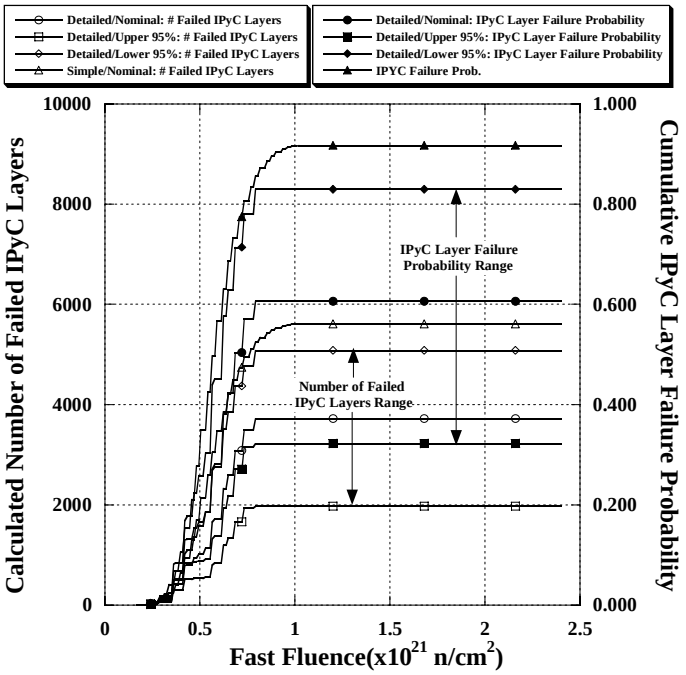

FIGURE 24. Compact NPR1-A8 calculated IPyC failure vs. fast fluence.

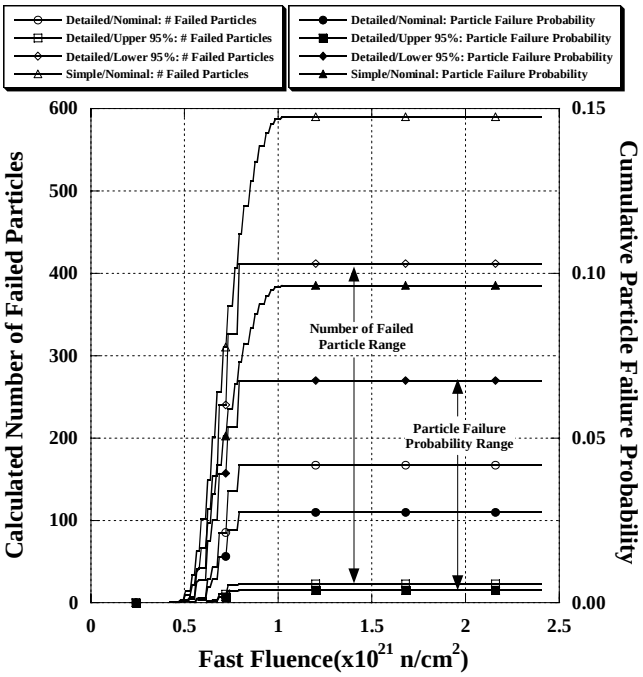

FIGURE 25. Compact NPR1-A8 calculated particle failure vs. fast fluence.

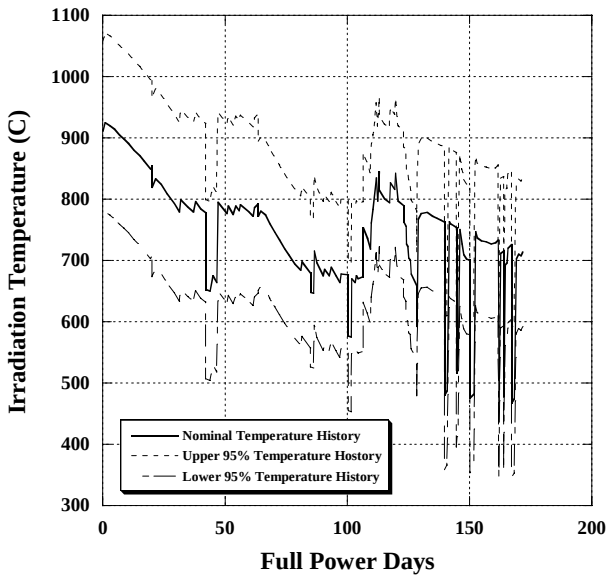

FIGURE 26. Temperature history for compact NPR2-A4 showing upper and lower 95% temperatures.

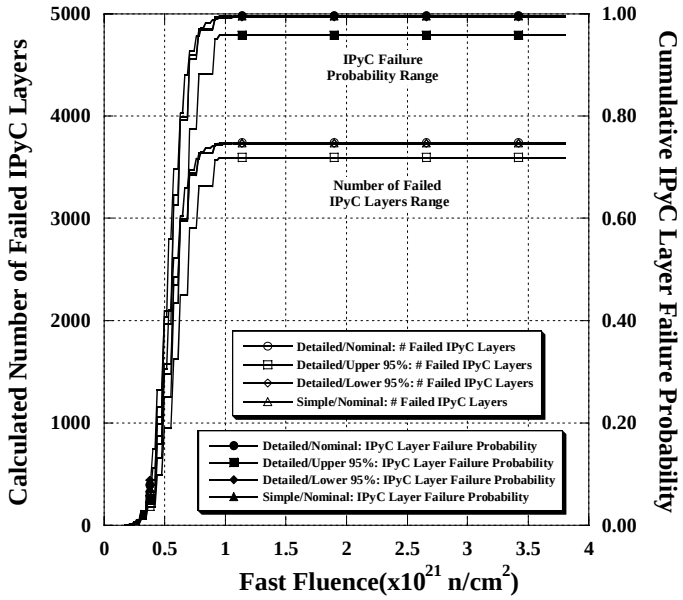

FIGURE 27. Compact NPR2-A4 calculated IPyC failure vs. fast fluence.

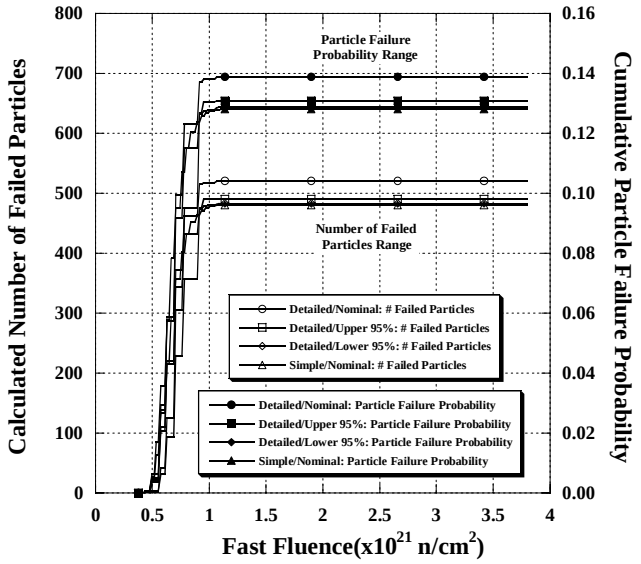

FIGURE 28. Compact NPR2-A4 calculated particle failure vs. fast fluence.

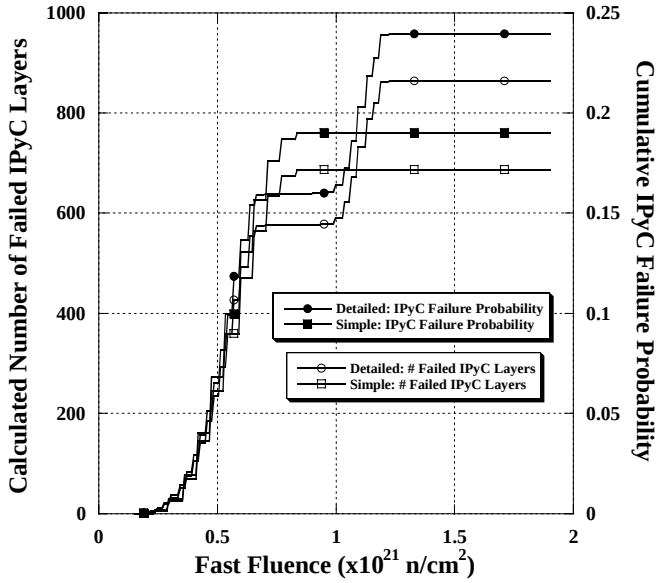

FIGURE 29. Compact NPR1A-A9 calculated IPyC failure vs. fast fluence.

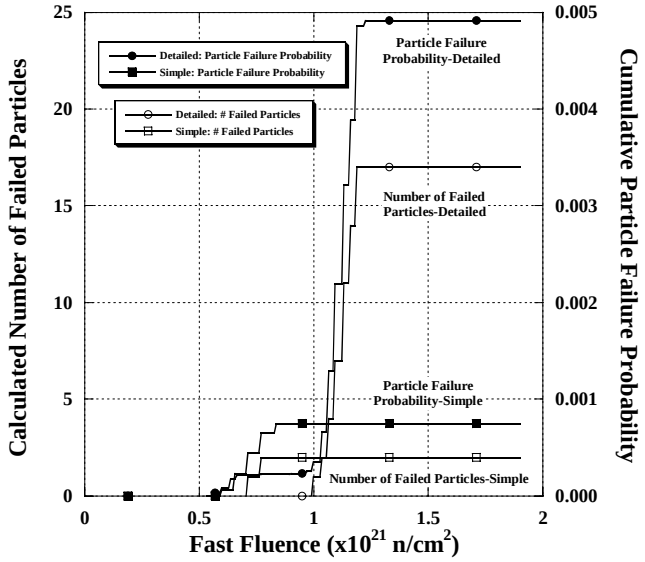

FIGURE 30. Compact NPR1A-A9 calculated particle failure vs. fast fluence.

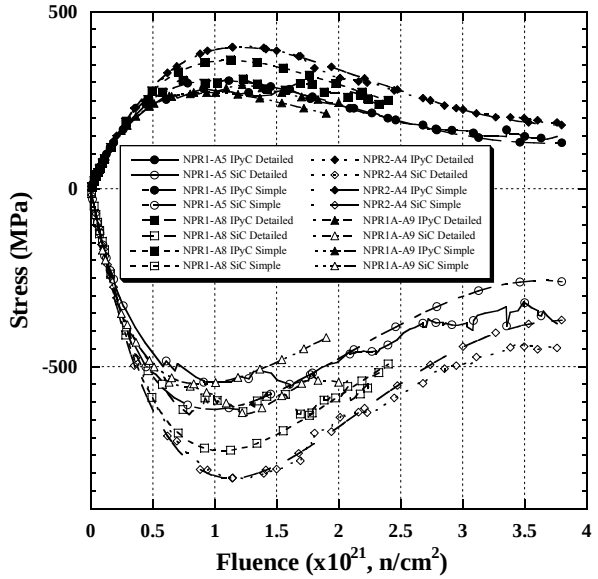

FIGURE 31. Calculated stress evolution for compacts NPR1-A5, A8, NPR1A-A9, and NPR2-A4.

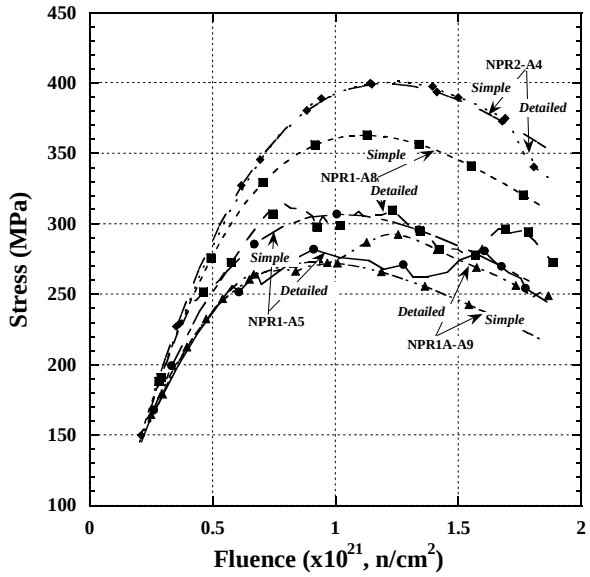

FIGURE 32. Expanded calculated stress evolution for compacts NPR1-A5, A8, NPR1A-A9, and NPR2-A4

ACKNOWLEDGMENTS

Much of the work reported here was funded as a part of a cooperative research program between MIT and the Idaho National Engineering and Environmental Laboratory.

REFERENCES

1. "Pre-qualification request: The Pebble Bed Modular Reactor", ESKOM, PBMR, IST Industrial, 1998.

2. G. K. Miller et al., "Consideration of the Effects on Fuel Particle Behavior from Shrinkage Cracks in the Inner Pyrocarbon Layer", Journal of Nuclear Materials 295, 205-212 (2001).

3. K. Sawa, K. Minato, "An Investigation of Irradiation Performance of High Burnup HTGR Fuel", Journal of Nuclear Science & Technology 36, No. 9, 781-791 (1999)

4. "Plan for Resolving Policy Issues Related to Licensing of Non-Light Water Reactor Designs", NRC SECY-02-0139, July 22, 2002.

5. R. K. McCardell, D. A. Petti, et al., "NP-MHTGR Fuel Development Program Results", 1993.

6. IAEA Technical Document, "Current Status and Future Development of Modular High Temperature Gas Cooled Reactor Technology", IAEA-TECDOC-1198, February 2001

7. G. Miller and R. Bennett, Journal of Nuclear Materials 206, 35-49 (1993)

8. D. Petti, et al., "Development of Improved Models and Designs for Coated-Particle Fuels", INEEL/EXT-02-00369, March 2002.

9. E. Techert, et al., "V.S.O.P (94) Computer Code System for Reactor Physics and Fuel Cycle Simulation", Forschungszentrum, Julich GmbH (Jul-2897), April 1994.

10. D. Dobranich, "Heat Transfer and Thermal Stress Analysis of the Multilayerd Spherical Particles of a Particle Bed Space Reactor", SAND90-1032, 1991.

11. M.M. El-Wakil, Nuclear Heat Transport, 104, The American Nuclear Society, 1993.

12. R.J. Price, "Thermal Conductivity of Neutron-Irradiated Pyrolytic β-Silicon Carbide", Journal of Nuclear Materials, 46, 268 (1973)

13. M.J. Kania, H. Nickel, "Performance Assessment of the $(Th,U)O_2$ HTI-BISO Coated Particle Under PNP/HHT Irradiation Conditions", JUL-1685, 1980.

14. A. F. Mills, Heat and Mass Transfer, Irwin, 1995.

15. P. R. Kasten, et al., "Fuel Performance in Modular High-Temperature Gas-Cooled Reactors", Interner Bericht·KFA-ISR-IB-12/94, October 1994.

16. W. J. Kovacs, et al., "High-Temperature Gas-Cooled Reactor Fuel Pressure Vessel Performance Models", Nuclear Technology 68, 344 (1985).

17. F. Ho, et al., "Material Models of Pyrocarbon and Pyrolytic Silicon Carbide", CEGA-002820, July 1993.

18. J. L. Kaae, "On Irradiation-Induced Creep of Pyrolytic Carbon in a General State of Stress", Journal of Nuclear Materials 34, 206-208 (1970).

19. J. C. Bokros, Carbon 3, 17 (1965)

20. R. K. McCardell, et al., "NP-MHTGR Fuel Development Program Plan, EGG-NPR-8971, Rev. C, September 1992.

21. J. L. Kaae, et al., "The Mechanical Behavior of Biso-Coated Fuel Particles During Irradiation, Part II: Prediction of Biso Particle Behavior During Irradiation with a Stress Analysis Model," Nuclear Technology 35, 368 (1977)

22. K. Bongartz, et al., "The Brittle Ring Test: A Method for Measuring Strength and Young's Modulus on Coatings of HTR Fuel Particles", Journal of Nuclear Materials 62, 123 (1976).

23. Material Specification No. SC-001, Morton Advanced Materials, 185 New Boston Street, Woburn, MA 01801

24. K. Sawa, et al., Journal of Nuclear Science & Technology 33, No. 9, 712-720, (1996).

25. R. G. Bennett, G. K. Miller, H. L. Menke, "User's Manual for the NP-MHTGR Fuel Code", EG&G Idaho, Inc., Idaho National Engineering and Environmental Laboratory, 1993.

26. C. A. Baldwin, R. R. Hobbins, et al., "The New Production Reactor Fuel Post Irradiation Examination Data Report for Capsules NPR1, NPR2, and NPR1A", ORNL/M-2849, Sept. 1993.

27. D. A. Petti, J. T. Maki, J. Buongiorno, R. R. Hobbins, and G. K. Miller, "Key Differences in the Fabrication, Irradiation and Safety Testing of US and German TRISO-coated Particle Fuel and their Implications on Fuel Performance", INEEL/EXT-02-00300, June 2002.